(12) INTERNATIONAL APPLICATION PUBLISHED UNDER THE PATENT COOPERATION TREATY (PCT)

(19) World Intellectual Property Organization
International Bureau

(43) International Publication Date
02 January 2025 (02.01.2025)

WIPO | PCT

(10) International Publication Number
WO 2025/007130 A2

(51) International Patent Classification:
A61N 5/06 (2006.01)

(21) International Application Number:
PCT/US2024/036401

(22) International Filing Date:
01 July 2024 (01.07.2024)

(25) Filing Language: English

(26) Publication Language: English

(30) Priority Data:
63/524,485 30 June 2023 (30.06.2023) US

(71) Applicant: **THE GEORGE WASHINGTON UNIVERSITY** [US/US]; 1922 F Street, NW, Washington, District of Columbia 20052 (US).

(72) Inventors: **LU, Luyao**; 7928 Robinson Rd., Bethesda, Maryland 20817 (US). **EFIMOV, Igor R.**; 514 N. Peshtigo Ct., Apt. 3305, Chicago, Illinois 60611 (US).

(74) Agent: **WEISSMAN, Peter S.**; BLANK ROME LLP, 1825 Eye Street NW, Washington, District of Columbia 20006 (US).

(81) Designated States *(unless otherwise indicated, for every kind of national protection available)*: AE, AG, AL, AM, AO, AT, AU, AZ, BA, BB, BG, BH, BN, BR, BW, BY, BZ, CA, CH, CL, CN, CO, CR, CU, CV, CZ, DE, DJ, DK, DM, DO, DZ, EC, EE, EG, ES, FI, GB, GD, GE, GH, GM, GT, HN, HR, HU, ID, IL, IN, IQ, IR, IS, IT, JM, JO, JP, KE, KG, KH, KN, KP, KR, KW, KZ, LA, LC, LK, LR, LS, LU, LY, MA, MD, MG, MK, MN, MU, MW, MX, MY, MZ, NA, NG, NI, NO, NZ, OM, PA, PE, PG, PH, PL, PT, QA, RO, RS, RU, RW, SA, SC, SD, SE, SG, SK, SL, ST, SV, SY, TH, TJ, TM, TN, TR, TT, TZ, UA, UG, US, UZ, VC, VN, WS, ZA, ZM, ZW.

(84) Designated States *(unless otherwise indicated, for every kind of regional protection available)*: ARIPO (BW, CV, GH, GM, KE, LR, LS, MW, MZ, NA, RW, SC, SD, SL, ST, SZ, TZ, UG, ZM, ZW), Eurasian (AM, AZ, BY, KG, KZ, RU, TJ, TM), European (AL, AT, BE, BG, CH, CY, CZ, DE, DK, EE, ES, FI, FR, GB, GR, HR, HU, IE, IS, IT, LT, LU, LV, MC, ME, MK, MT, NL, NO, PL, PT, RO, RS, SE, SI, SK, SM, TR), OAPI (BF, BJ, CF, CG, CI, CM, GA, GN, GQ, GW, KM, ML, MR, NE, SN, TD, TG).

Declarations under Rule 4.17:
— *of inventorship (Rule 4.17(iv))*

Published:
— *without international search report and to be republished upon receipt of that report (Rule 48.2(g))*

(54) **Title:** SOFT, BIORESORBABLE, TRANSPARENT MICROELECTRODE ARRAY FOR CARDIAC APPLICATIONS

(57) **Abstract:** Transparent microelectrode arrays (MEAs) that allow multimodal investigation of the spatiotemporal cardiac characteristi cs are important in studying and treating heart disease. Existing implantable devices, however, are designed to support chronic operational lifetimes and require surgical extraction when they malfunction or are no longer needed. Meanwhile, bioresorbable systems that can self-eliminate after performing temporary functions are increasingly attractive because they avoid the costs/risks of surgical extraction. Here, we provide a design, fabrication, characterization, and validation of a soft, fully bioresorbable, and transparent MEA platform for bidirectional cardiac interfacing over a clinically relevant period. The MEA provides multiparametric electrical/optical mapping of cardiac dynamics and on-demand site-specific pacing to investigate and treat cardiac dysfunctions in rat and human heart models. The bioresorption dynamics and biocompatibility are investigated. The device designs serve as the basis for bioresorbable cardiac technologies for potential postsurgical monitoring and treating temporary patient pathological conditions in certain clinical scenarios, such as myocardial infarction, ischemia, and transcatheter aortic valve replacement.

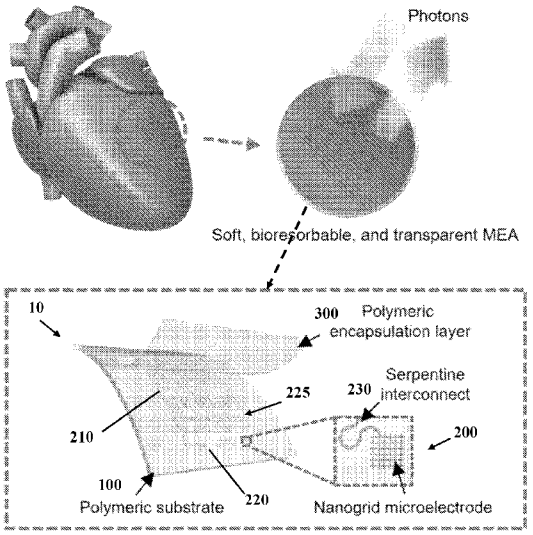


FIGURE 1A

WO 2025/007130 A2

SOFT, BIORESORBABLE, TRANSPARENT MICROELECTRODE ARRAY FOR CARDIAC APPLICATIONS

GOVERNMENT LICENSE RIGHTS

[0001] This invention was made with government support under Grant Nos. 2011093 and 2131682, awarded by NSF, and Grant No. R01 HL141470 awarded by NIH. The government has certain rights in the invention.

RELATED APPLICATION

[0002] This application claims the benefit of U.S. Provisional Application No. 63/524,485, filed June 30, 2023, the entire contents of which are incorporated herein by reference. The references cited in the provisional application are also hereby incorporated by reference in their entireties herein.

BACKGROUND

[0003] Heart disease costs the United States ~$219 billion annually, with ~655,000 Americans dying from heart disease each year (about 1 in 4 deaths). A contributing factor underlying these surprisingly grim numbers is the lack of tools that can spatiotemporally map and control the cardiac metabolic and electromechanical activity to unravel the complex pathophysiology of heart disease, provide intraoperative or postsurgical recovery monitoring, and develop effective and timely clinical treatments. Microelectrode arrays (MEAs) are generally used in medical devices to obtain neural signals from and/or deliver therapeutic signals to the body, such as tissue. Noble metal (e.g., platinum (Pt), iridium) based MEAs are widely used to probe the patterns of cardiac excitation waves and identify the regions that are responsible for cardiac arrhythmias while electrical cardiac pacemakers and defibrillators are the cornerstone of therapy used in clinical medicine to correct the abnormal heart rhythm. See R. G. Trohman, M. H. Kim, S. L. Pinski, Cardiac pacing: the state of the art. *Lancet* **364**, 1701-1719 (2004). M. E. Spira, A. Hai, Multi-electrode array technologies for neuroscience and cardiology. *Nat. Nanotechnol.* **8**, 83-94 (2013). J. S. Choi, H. J. Lee, S. Rajaraman, D.-H. Kim, Recent advances in three-dimensional microelectrode array technologies for in vitro and in vivo cardiac and neuronal interfaces. *Biosens. Bioelectron.* **171**, 112687 (2021).

[0004] However, they are problematic in probing important cardiac parameters such as intracellular calcium dynamics, metabolic activity, or target specific cell types. Optical

mapping using voltage/calcium-sensitive fluorescent dyes or intrinsic fluorescence complements these electrical approaches and reveals the roles of the aforementioned cellular parameters during cardiac function in health and disease. S. A. George, I. R. Efimov, Optocardiography: A review of its past, present, and future. Curr. Opin. Biomed. Eng. 9, 74-80 (2019).

[0005] Recent developments in optically transparent MEAs based on graphene, carbon nanotubes (CNTs), conductive polymers, gold (Au) nanostructures have allowed light to transmit through the microelectrodes in both directions for co-localized crosstalk-free electrophysiology and optical mapping to take the full advantages of each technique. D. Kuzum, H. Takano, E. Shim, J. C. Reed, H. Juul, A. G. Richardson, J. de Vries, H. Bink, M. A. Dichter, T. H. Lucas, D. A. Coulter, E. Cubukcu, B. Litt, Transparent and flexible low noise graphene electrodes for simultaneous electrophysiology and neuroimaging. Nat. Commun. 5, 5259 (2014). D.-W. Park, A. A. Schendel, S. Mikael, S. K. Brodnick, T. J. Richner, J. P. Ness, M. R. Hayat, F. Atry, S. T. Frye, R. Pashaie, S. Thongpang, Z. Ma, J. C. Williams, Graphene-based carbon-layered electrode array technology for neural imaging and optogenetic applications. Nat. Commun. 5, 5258 (2014). J. Zhang, X. Liu, W. Xu, W. Luo, M. Li, F. Chu, L. Xu, A. Cao, J. Guan, S. Tang, X. Duan, Stretchable Transparent Electrode Arrays for Simultaneous Electrical and Optical Interrogation of Neural Circuits in Vivo. *Nano Lett.* **18**, 2903-2911 (2018). Y. U. Cho, J. Y. Lee, U.-J. Jeong, S. H. Park, S. L. Lim, K. Y. Kim, J. W. Jang, J. H. Park, H. W. Kim, H. Shin, H. Jeon, Y. M. Jung, I.-J. Cho, K. J. Yu, Ultra-Low Cost, Facile Fabrication of Transparent Neural Electrode Array for Electrocorticography with Photoelectric Artifact-Free Optogenetics. *Adv. Funct. Mater.* **32**, 2105568 (2022). Y. Qiang, P. Artoni, K. J. Seo, S. Culaclii, V. Hogan, X. Zhao, Y. Zhong, X. Han, P.-M. Wang, Y.-K. Lo, Y. Li, H. A. Patel, Y. Huang, A. Sambangi, J. S. V. Chu, W. Liu, M. Fagiolini, H. Fang, Transparent arrays of bilayer-nanomesh microelectrodes for simultaneous electrophysiology and two-photon imaging in the brain. *Sci. Adv.* **4**, eaat0626 (2018). S. N. Obaid, R. T. Yin, J. Tian, Z. Chen, S. W. Chen, K. B. Lee, N. Boyajian, A. N. Miniovich, I. R. Efimov, L. Lu, Multifunctional Flexible Biointerfaces for Simultaneous Colocalized Optophysiology and Electrophysiology. *Adv. Funct. Mater.* **30**, 1910027 (2020). L. Lu, Recent Progress on Transparent Microelectrode-Based Soft Bioelectronic Devices for Neuroscience and Cardiac Research. *ACS Appl. Bio Mater.* **6**, 1701-1719 (2023).

[0006] In addition, optically transparent MEAs are highly desired during clinical processes to allow direct observation of areas of interest under the microelectrode sites for concurrent

optical diagnostics/therapies (e.g., endoscopy) and guiding other procedures (e.g., catheters) on the hearts. Meanwhile, all current transparent MEAs are designed to exhibit long-term reliable performance for chronic biointerfacing. T.-K. Nguyen, S. Yadav, T.-A. Truong, M. Han, M. Barton, M. Leitch, P. Guzman, T. Dinh, A. Ashok, H. Vu, V. Dau, D. Haasmann, L. Chen, Y. Park, T. N. Do, Y. Yamauchi, J. A. Rogers, N.-T. Nguyen, H.-P. Phan, Integrated, Transparent Silicon Carbide Electronics and Sensors for Radio Frequency Biomedical Therapy. *ACS Nano* **16**, 10890-10903 (2022).

[0007] Bioresorbable is any material that can be absorbed by the body. Bioresorbable materials are used in medical applications, such as sutures, so that they do not need to be manually removed from the body. They typically degrade over a period of time.

[0008] Bioresorbable electronics offer unique opportunities to investigate, monitor, and treat short-lived cardiac complications, such as postoperative arrhythmias and heart failure on the order of a few days to weeks following ischemic events or surgery, which account for at least one-third of postoperative deaths. Those devices can subsequently dissolve into benign products via natural metabolic mechanisms to avoid complications from surgical retrieval of the implants, lower infection risks, and eliminate additional financial burdens to patients. For example, removal of the temporary pacing devices following completion of therapy can cause laceration and perforation of the myocardium. There has been much recent work on soft bioresorbable electronic devices. Examples include cardiac pacemakers to treat cardiac arrhythmias, peripheral nerve stimulators for pain block, electrical sensors to map activity from the cerebral cortex or record physiological signals, electrotherapy systems to provide electrostimulation and impedance sensing, chemical sensors to monitor critical biomarkers in various organs, etc. See Y. S. Choi, R. T. Yin, A. Pfenniger, J. Koo, R. Avila, K. Benjamin Lee, S. W. Chen, G. Lee, G. Li, Y. Qiao, A. Murillo-Berlioz, A. Kiss, S. Han, S. M. Lee, C. Li, Z. Xie, Y.-Y. Chen, A. Burrell, B. Geist, H. Jeong, J. Kim, H.-J. Yoon, A. Banks, S.-K. Kang, Z. J. Zhang, C. R. Haney, A. V. Sahakian, D. Johnson, T. Efimova, Y. Huang, G. D. Trachiotis, B. P. Knight, R. K. Arora, I. R. Efimov, J. A. Rogers, Fully implantable and bioresorbable cardiac pacemakers without leads or batteries. *Nat. Biotechnol.* **39**, 1228-1238 (2021). G. Lee, E. Ray, H.-J. Yoon, S. Genovese, Y. S. Choi, M.-K. Lee, S. Şahin, Y. Yan, H.-Y. Ahn, A. J. Bandodkar, J. Kim, M. Park, H. Ryu, S. S. Kwak, Y. H. Jung, A. Odabas, U. Khandpur, W. Z. Ray, M. R. MacEwan, J. A. Rogers, A bioresorbable peripheral nerve stimulator for electronic pain block. *Sci. Adv.* **8**, eabp9169 (2022). K. J. Yu, D. Kuzum, S.-W. Hwang, B. H. Kim, H. Juul, N. H. Kim, S. M. Won, K. Chiang, M. Trumpis, A. G.

Richardson, H. Cheng, H. Fang, M. Thompson, H. Bink, D. Talos, K. J. Seo, H. N. Lee, S.-K. Kang, J.-H. Kim, J. Y. Lee, Y. Huang, F. E. Jensen, M. A. Dichter, T. H. Lucas, J. Viventi, B. Litt, J. A. Rogers, Bioresorbable silicon electronics for transient spatiotemporal mapping of electrical activity from the cerebral cortex. *Nat. Mater.* **15**, 782-791 (2016). H. Zhao, Z. Xue, X. Wu, Z. Wei, Q. Guo, M. Xu, C. Qu, C. You, Y. Mei, M. Zhang, Z. Di, Q. Guo, Biodegradable germanium electronics for integrated biosensing of physiological signals. *npj Flex. Electron.* **6**, 63 (2022). J. W. Song, H. Ryu, W. Bai, Z. Xie, A. Vázquez-Guardado, K. Nandoliya, R. Avila, G. Lee, Z. Song, J. Kim, M.-K. Lee, Y. Liu, M. Kim, H. Wang, Y. Wu, H.-J. Yoon, S. S. Kwak, J. Shin, K. Kwon, W. Lu, X. Chen, Y. Huang, G. A. Ameer, J. A. Rogers, Bioresorbable, wireless, and battery-free system for electrotherapy and impedance sensing at wound sites. *Nat. Commun.* **9**, eade4687 (2023). R. Li, H. Qi, Y. Ma, Y. Deng, S. Liu, Y. Jie, J. Jing, J. He, X. Zhang, L. Wheatley, C. Huang, X. Sheng, M. Zhang, L. Yin, A flexible and physically transient electrochemical sensor for real-time wireless nitric oxide monitoring. *Nat. Commun.* **11**, 3207 (2020).

[0009] However, developments in soft transparent MEAs that exhibit bioresorbable functionality remain limited and challenging.

SUMMARY

[0010] The present disclosure provides materials, device designs, fabrication strategies, performance characteristics, ex vivo and in vivo demonstrations, and systematic biocompatibility assessments of a fully bioresorbable, implantable, flexible, and transparent MEA technology that can provide organ conformal cardiac interfacing over clinically relevant temporary timescales. The devices integrate entirely Food and Drug Administration approved materials that will completely disappear through natural biological processes in the body after a desired period of use.

BRIEF DESCRIPTION OF THE FIGURES

[0011] FIGS. 1A-1H show a soft, bioresorbable, and transparent MEA for multimodal electrical and optical cardiac interrogation.

[0012] FIG. 1A is a schematic illustration of a MEA on a heart. The device comprises Mo nanogrid microelectrodes and interconnects, PLGA encapsulation and substrate layers.

[0013] FIG. 1B are optical images of the MEA to show transparency (left) and flexibility (right).

[0014] FIG. 1C is a scanning electron microscopy (SEM) image of the Mo nanogrid structure. Grid width: 500 nm. Grid thickness: 1000 nm.

[0015] FIG. 1D is a graph of a transmission spectra of the Mo nanogrids (pitch: 6.75 μm) at various thicknesses.

[0016] FIG. 1E is a graph of a transmission spectra of the Mo nanogrids (thickness: 1000 nm) at various pitch values.

[0017] FIG. 1F shows dissolution kinetics of 1000 nm-thick Mo layers in 1× PBS at 37, 60, and 90 °C, evaluated as decreases in thicknesses.

[0018] FIGS. 1G, 1H are optical images of the MEA device at various dissolution stages in 1× PBS at 37 °C.

[0019] FIGS. 2A-2I show electrochemical characterization of Mo nanogrid microelectrodes and MEAs.

[0020] FIG. 2A shows impedance spectra of Mo nanogrid microelectrodes (pitch: 6.75 μm) at various thicknesses.

[0021] FIG. 2B shows impedance spectra of Mo nanogrid microelectrodes (thickness: 1000 nm) at various pitch values.

[0022] FIG. 2C shows 1 kHz impedance values of Mo nanogrid microelectrodes as a function of microelectrode sizes.

[0023] FIG. 2D is a phase plot of the Mo nanogrid microelectrode.

[0024] FIG. 2E shows normalized impedance versus transmittance comparison of different transparent microelectrode materials for electrophysiological studies where the Mo nanogrid microelectrode is the only bioresorbable one.

[0025] FIG. 2F shows CV curves of a Mo nanogrid microelectrode at various scan rates.

[0026] FIG. 2G shows impedance spectra of all 16 Mo nanogrid microelectrodes in a MEA. Inset: 1 kHz impedance colormap of the microelectrodes relative to the actual microelectrode position in the MEA.

[0027] FIG. 2H is a CSC_c histogram of 16 Mo nanogrid microelectrodes in a MEA at the scan rate of 50 mV/s. Inset: CSC_c colormap of the microelectrodes relative to the actual microelectrode position in the MEA.

[0028] FIG. 2I shows impedance of a Mo nanogrid MEA as a function of bending cycles at 1 cm radius. Z and Z_0 represent the impedance value at a specific bending cycle and the initial impedance, respectively.

[0029] FIGS. 3A-3F show benchtop measurements of Mo nanogrid microelectrodes and MEAs.

[0030] FIG. 3A is a representative output recording of a Mo nanogrid microelectrode during a 10 Hz, 20 mV peak-to-peak amplitude sine wave input delivered by a Pt electrode in PBS.

[0031] FIG. 3B is a representative PSD curve of the recorded signals in (A).

[0032] FIG. 3C is a histogram of calculated SNRs of 16 microelectrodes in a MEA. Inset: SNR colormap of the microelectrodes relative to the actual microelectrode position in the MEA.

[0033] FIG. 3D is a histogram of calculated RMS noises of 16 microelectrodes in a MEA. Inset: RMS noise colormap of the microelectrodes relative to the actual microelectrode position in the MEA.

[0034] FIG. 3E shows changes in impedance (black line) and CSC_c (red line) during dissolution in PBS at 37 °C. Z and CSC_c represent the impedance and CSC_c value at a specific day while Z_0 and $(CSC_c)_0$ represent the initial impedance and CSC_c, respectively.

[0035] FIG. 3F are impedance curves and equivalent circuit model fittings of the MEAs at different dissolution stages on Day 0 and 4, respectively.

[0036] FIGS. 4A-G are an *Ex vivo* demonstration of the MEA for simultaneous co-localized electrical/optical interrogation of rat hearts and human ventricular slices.

[0037] FIG. 4A Top is a schematic illustration of EG mapping (from the MEAs) and optical dual mapping (V_m and Ca^{2+}) system. Bottom is a schematic illustration of simultaneous multi-level and multiparametric mapping in the same field of view.

[0038] FIG. 4B is a synchronous and co-localized EG, V_m, and Ca^{2+} traces recorded from different cardiac tissue regions beneath the transparent microelectrodes of the MEA during sinus rhythm. Green box: Zoomed in view of three overlapping traces at each microelectrode of the MEA.

[0039] FIG. 4C are concurrent V_m (left), EG (middle) and Ca^{2+} (right) activation maps during sinus rhythm. The white square represents the region covered by the transparent MEA.

[0040] FIG. 4D are concurrent V_m (left), EG (middle) and Ca^{2+} (right) activation maps during MEA pacing. The pacing site is marked with yellow lightning bolts.

[0041] FIG. 4E are QRS complexes (black line) recorded by the MEAs at various dissolution stages in PBS at 37 °C, and correlated SNRs (red symbol). The QRS complexes are recorded from the same rat heart.

[0042] FIG. 4F Left is a schematic illustration of the region where the human ventricular slices are collected. Right is an optical image of the MEA on a human cardiac slice to show transparency.

[0043] FIG. 4G is a camera view of the MEA on a human cardiac slice (left), V_m (middle) and EG (right) activation maps.

[0044] FIGS. 5A-5F show an *In vivo* demonstration of the MEA for simultaneous electrical monitoring and pacing for arrhythmias management.

[0045] FIG. 5A is an optical image of the MEA contacting the left ventricle of a blood-perfused rat heart to show transparency and flexibility.

[0046] FIG. 5B Left is a schematic illustration of the electrical mapping location of the MEA on a rat heart (front-lateral side of the left ventricle). Right is an electrical activation map generated by the MEA during sinus rhythm.

[0047] FIG. 5C are electrical activation maps from the MEA during unipolar pacing at different sites. The pacing sites are marked with yellow lightning bolts. The red arrow represents the direction of cardiac wave propagation.

[0048] FIG. 5D is an electrical activation map from the MEA during bipolar pacing with two neighboring microelectrodes in the MEA.

[0049] FIG. 5E is a demonstration of MEA multi-channel sensing and pacing capabilities for arrhythmias monitoring and treatment. Orange box: Simultaneous EG recording and bipolar pacing from the MEA during 3:1 AV block. Green box: Zoomed in view of the 3:1 AV block recorded by far-field ECG. The location of AV block (cartoon).

[0050] FIG. 5F show QRS complexes (black line) recorded by the bioresorbable MEAs at various dissolution stages in PBS at 37 °C, and correlated SNRs (red symbol). The QRS complexes are recorded from the same rat heart.

[0051] FIGS. 6A-6J show an *In vivo* bioresorption, histology, biocompatibility, and serology test.

[0052] FIG. 6A are optical images of the rat hearts *in situ* (square box) and after explantation (circular box).

[0053] FIG. 6B are representative histology images of Masson's trichrome staining of cardiac tissues. Red: Cardiomyocytes staining. Blue: Fibrosis staining. White: Interstitial space

staining. Devices are stitched over the epicardium (the green triangle indicates the epicardial side).

[0054] FIG. 6C are quantified volume percentage of the cardiomyocytes, fibrosis, and interstitial space in FIG. 6B. No statistically significant difference is found among different groups.

[0055] FIG. 6D is a transthoracic echocardiogram test on the stroke volume and ejection function of the heart at different time points after implantation. No statistically significant difference is found.

[0056] FIG. 6E is a weight measurement of the animals at different time points after implantation. A normal weight loss is observed immediately after the surgery and is followed by a gradual weight gain resulting from a natural increase in age. Serology test of biomarkers for the evaluation of the function of heart (FIG. 6F), liver (FIG. 6G), kidney (FIG. 6H), and the level of inflammation (FIG. 6I) and electrolyte (FIG. 6J). No statistically significant difference is found among different groups. Data are presented with error bars as means ± S.D. The statistical comparison among different groups is calculated with a nonparametric Kruskal-Wallis test in conjunction with Dunn's multiple comparison tests at a significance level of $P < 0.05$. $n = 3$ animals per group.

[0057] FIG. 7 is a schematic illustration of the fabrication process for the soft, bioresorbable, transparent Mo nanogrid MEA.

[0058] FIGS. 8A-8C show a soft, bioresorbable, transparent Mo microgrid microelectrodes via photolithography.

[0059] FIG. 8A is an optical image of Mo microgrids on PLGA with a grid width of 8 μm and pitch of 144 μm.

[0060] FIG. 8B is a representative transmittance spectrum for FIG. 8A.

[0061] FIG. 8C is an impedance curve of the Mo microgrid microelectrodes in FIG. 8A.

[0062] FIG. 9 are SEM images of the Mo nanogrids on PLGA substrates at different dissolution stages (Week 0, 2 and 5).

[0063] FIGS. 10A, 10B are HRTEM images.

[0064] FIG. 10A show EDS spectra of Mo.

[0065] FIG. 10B show at Day 0, 1, and 2, respectively.

[0066] FIGS. 11A-11D are a representative benchtop electrical output recording of 10 Hz sine waves at various amplitudes in PBS by the Mo nanogrid microelectrodes. The output

recording from sine wave inputs at the peak-to-peak amplitude of (FIG. 11A) 2 mV, (FIG. 11B) 1 mV, (FIG. 11C) 200 μV, (FIG. 11D) 100 μV.

[0067] FIG. 12 is a 10 Hz impedance histogram of 16 Mo nanogrid microelectrodes in a MEA. Inset: 10 Hz impedance colormap of the microelectrodes relative to the actual microelectrode position in the MEA.

[0068] FIGS. 13A-13H show SNRs and RMS noises of 4 additional MEAs. (FIGS. 13A-13D) Histograms of calculated SNRs of 64 microelectrodes in 4 additional MEAs. Inset: SNR colormap of the microelectrodes relative to the actual microelectrode position in the MEA. (FIGS. 13E-13H) Histograms of calculated RMS noises of 64 microelectrodes in 4 additional MEAs. Inset: RMS noise colormap of the microelectrodes relative to the actual microelectrode position in the MEA.

[0069] FIG. 14 is an equivalent circuit model for Mo nanogrid microelectrode EIS simulation.

[0070] FIG. 15 shows MEA activation maps during AV block without and with bipolar pacing using the MEA.

[0071] FIGS. 16A-16D are representative QRS complexes recorded by gold microelectrodes on Langendorff perfused rat hearts during sinus rhythm.

[0072] FIGS. 17A-17F are an echocardiogram assessment of cardiac relaxation and contraction function of animals following the MEA implantation.

[0073] FIG. 17A shows diastolic volume is the volume of blood in the left ventricle at the end of ventricular filling.

[0074] FIG. 17B shows systolic volume is the volume of blood in the left ventricle at the end of ventricular contraction.

[0075] FIG. 17C shows cardiac output is the volume of blood pumped out by the left ventricle per minute.

[0076] FIG. 17D shows diastolic diameter is the diameter across the left ventricle at the end of diastole.

[0077] FIG. 17E shows systolic diameter is the diameter across the left ventricle at the end of systole.

[0078] FIG. 17F shows fractional shortening is the percentage of shortening in left ventricle diameter per cardiac contraction (*i.e.*, fractional shortening = (diastolic diameter - systolic diameter) / diastolic diameter). (FIGS. 17A-17F) Data are presented with error bars as means ± S.D. No statistically significant difference is found among different groups revealing

negligible effect on cardiac mechanical function after device implantation. n = 3 animals per group. The comparison is calculated with a nonparametric Kruskal-Wallis test in conjunction with Dunn's multiple comparison tests at a significance level of $P < 0.05$.

[0079] FIGS. 18A-18B show a serology test for liver function assessment. FIG. 18A shows analysis of total bilirubin and FIG. 18B shows albumin-to-globulin ratio reveals negligible effect on liver function in animals after device implantation. No statistically significant difference is found among different groups. n = 3 animals per group. Data are presented with error bars as means ± S.D. The comparison is calculated with a nonparametric Kruskal-Wallis test in conjunction with Dunn's multiple comparison tests at a significance level of $P < 0.05$.

[0080] FIGS. 19A-19D are a serology test for inflammation assessment. Analysis of (FIG. 19A) red blood cells, (FIG. 19B) basophils, (FIG. 19C) monocytes, and (FIG. 19D) eosinophils reveals similar inflammation levels in animals with and without device implantation. No statistically significant difference is found among different groups. n = 3 animals per group. Data are presented with error bars as means ± S.D. The comparison is calculated with a nonparametric Kruskal-Wallis test in conjunction with Dunn's multiple comparison tests at a significance level of $P < 0.05$.

[0081] FIGS. 20A, 20B show a mechanical bending test system. FIG. 20A is an optical image of the motorized test stand. FIG. 20B is a zoomed in image of a device on the test machine.

[0082] FIG. 21 is a system for electrochemical characterizations.

[0083] FIG. 22 is a system for optical mapping of the human cardiac tissue slices.

DETAILED DESCRIPTION

[0084] In describing the preferred embodiments of the present disclosure illustrated in the drawings, specific terminology is resorted to for the sake of clarity. However, the present disclosure is not intended to be limited to the specific terms so selected, and it is to be understood that each specific term includes all technical equivalents that operate in a similar manner to accomplish a similar purpose.

[0085] Design of bioresorbable and transparent Mo nanogrid MEA

[0086] FIG. 1A is a non-limiting illustrative embodiment of a medical detection and treatment device 10, and more specifically a microelectrode array (MEA) device or assembly 10, in accordance with an example embodiment of the present disclosure. The assembly 10

has a substrate layer 100, an active layer 200, and an encapsulation layer 300. The entire assembly 10 is bioresorbable, wherein the substrate layer 100, active layer 200, and encapsulation layer 300 are each made of a bioresorbable material, so that the assembly 10 is dissolved or absorbed by the body after a period of time, and need not be manually removed from the body. In addition, the entire assembly 10 is optically transparent. Accordingly, the bioresorbable material for each of the substrate layer 100, active layer 200, and encapsulation layer 300 is transparent. And, the entire assembly 10 is flexible so that the assembly 10 can bend in half so that opposite ends come together. Accordingly, the bioresorbable material for each of the substrate layer 100, active layer 200, and encapsulation layer 300 is flexible.

[0087] The substrate layer 100 is optically transparent and flexible, and is made of a bioresorbable material. The substrate 100 retains and provides structural support to the active layer 200, and so can be thicker (thickness: 90 μm) than the encapsulation layer 300. In one embodiment, the bioresorbable substrate material is polylactic-co-glycolic acid (PLGA).

[0088] The active layer 200 includes the electronic components of the assembly 10, and is coupled to the substrate layer 100. In one embodiment, the electronic components include a metal grid 210, and an array of one or more electrodes 220. In some embodiments, the grid can optionally have a structural purpose to hold the electrodes in position, and an electrical purpose to communicate signals to/from the electrodes. In some embodiments, the electrodes 220 can form an integral part of the metal grid 210, and in other embodiments the electrodes 220 can be separate components and coupled (e.g., a fastener) or affixed (e.g., adhered) to the grid 210. The grid can have support bars that are arranged in columns and rows with spaces/voids therebetween and form a square, rectangular, or other shape. One or more interconnects 230 are provided, which can be serpentine or other shape. The interconnects 230 can electrically couple the electrodes 220 and/or grid 210 to an external electronic component, such as a signal regulator or signal analyzer, and extends from the grid 210 or electrode 220 to an electrical pad on the substrate 100 or at the edge of the substrate 100. The interconnects 230 carry electrical signals used to apply a therapy or treatment to the electrode 220 and/or to detect an electrical signal sensed by the electrode 220. The interconnects 230 can optionally be flexible, transparent, bioresorbtive, and can be metal. The interconnect 230 can be sufficiently thin to dissolve or pass out of the body once the other layers 100, 300 dissolve. One or more electrical pads are provided.

[0089] The active layer 200 can be formed in any suitable manner, such as an electron-beam lithography (EBL) patterned transparent molybdenum (Mo) nanogrid MEA, and a photolithography determined interconnect layer.

[0090] The encapsulation layer 300 is formed over the active layer 200, so that the active layer 200 is fixedly positioned between the substrate 100 and the encapsulation layer 300. The encapsulation layer 300 can be formed by a soft lithography defined transparent PLGA and can be thinner (thickness: 40 μm) than the substrate layer 100. In other embodiments, the substrate 100 can be the same or smaller thickness than the encapsulation layer 300, and the substrate 100 and encapsulation layer 300 need not both be made of the same material. The encapsulation layer 300 and substrate 100 provide a liquid-proof and touch-proof seal for the active layer 200, so that liquid does not interfere with operation of the active layer 200 and the active layer does not come into contact with the body. However, the substrate 100 and encapsulation layer 300 do not interfere with the operation of the active layer 200, so that for example the electrodes 200 can detect signals from the body and apply therapeutic signals to the body.

[0091] The assembly 10 can be prepared in any suitable manner, including that the nanoscale Mo structures can be based on metal grid approaches for preparing high-performance soft transparent MEAs, such as shown for example, in S. N. Obaid, R. T. Yin, J. Tian, Z. Chen, S. W. Chen, K. B. Lee, N. Boyajian, A. N. Miniovich, I. R. Efimov, L. Lu, Multifunctional Flexible Biointerfaces for Simultaneous Colocalized Optophysiology and Electrophysiology. *Adv. Funct. Mater.* **30**, 1910027 (2020); S. N. Obaid, Z. Chen, M. Madrid, Z. Lin, J. Tian, C. Humphreys, J. Adams, N. Daza, J. Balansag, I. R. Efimov, L. Lu, Flexible Electro-Optical Arrays for Simultaneous Multi-Site Colocalized Spatiotemporal Cardiac Mapping and Modulation. *Adv. Opt. Mater.* **10**, 2201331 (2022); and S. N. Obaid, N. Quirion, J. D. Torres Balansag, N. Daza, X. Shi, Z. Chen, L. Lu, Design and Fabrication of a Flexible Opto-Electric Biointerface for Multimodal Optical Fluorescence and Electrical Recording. *ACS Appl. Electron. Mater.* **5**, 1688-1696 (2023).

[0092] Studies on rat and human hearts highlight the function, form factor, durability, and capability of the devices for (1) co-localized multiparametric spatiotemporal electrical/optical mapping of critical cardiac physiological parameters, such as heart rhythm, biopotentials, oxygenation, metabolic state, calcium homeostasis, activation propagation pattern, and myocardial conduction and contraction; (2) real-time demand-based site-specific cardiac

pacing to control the propagations of cardiac waves and provide therapeutic solutions such as treating bradycardia and atrioventricular (AV) block on soft heart tissue surfaces.

[0093] Alternative pacing technologies, such as optogenetic or non-genetic optical pacing of the hearts, have also been widely used in cardiac research. Optogenetics is a promising optical pacing method that uses light-activated ion channels to control cardiac activity. However, it could be challenging to implement optogenetic pacing for clinical applications due to the requirement of gene transfection. Non-genetic optical pacing techniques use materials that can convert photons into electricity or heat to modulate the membrane potentials of cardiomyocytes. Those technologies mostly rely on external light sources for optical pacing with physically separated electrocardiogram (ECG) electrodes for monitoring the resulting cardiac activity, and could be difficult to accommodate concurrent optical mapping due to potential optical crosstalk.

[0094] Meanwhile, the MEA assembly 10 enables both single site and multisite pacing with simultaneous electrical cardiac mapping in detecting and treating cardiac complications, require no genetic labels, and avoid the potential optical crosstalk with co-localized optical mapping investigations, which are more suitable for future temporary non-toxic safe use in humans. The MEAs are stable for several days when immersed in phosphate-buffered saline (PBS), which is on par with many postoperative care cycles, followed by complete bioresorption via hydrolysis within 6 weeks in vivo. Taken together, this work establishes the foundations of a soft bioresorbable transparent MEA technology to greatly expand the landscape for bioresorbable transient electronics and complement traditional approaches, with the potential to address the unmet needs in fundamental and translational cardiac research (e.g., ablation and surgical intervention procedures, postoperative recovery monitoring, post-infarction recovery, post-transcatheter aortic valve replacement (TAVR) recovery) where transient mapping and control of cardiac physiological parameters and functions are required.

[0095] FIG. 1A shows one non-limiting illustrative example embodiment of the assembly 10. Here, the assembly 10 can be a plurality of microelectrodes 220 formed as a 4 × 4 array 225 that is attached to a nanogrid 210. The microelectrodes 220 are bidirectional and the array 225 is attached to the heart surface in any suitable manner, such a with bioresorbable sutures. The MEA device is optically transparent (FIG. 1B, left) and bendable / flexible (FIG. 1B, right). Each microelectrode features a nanogrid network structure with a thickness of 1000 nm, a grid width of 500 nm, and a pitch of 6.75 μm (FIG. 1C). The nanoscale dimensions enable adjusting the physical properties of the nanogrid network when scaling down the

microelectrode sizes. The void spaces between the nanogrids allow photons to pass through the microelectrodes 220 for co-localized optical operations. The edge-to-edge distance between two nearby microelectrodes 220 in the MEA 225 is determined by the electrophysiological space constant of cardiac tissue to achieve high spatial resolution electrical mapping and control of the cardiac signal propagation from the epicardium. The overall active MEA area (~5 × 5 mm^2) is on par with the sizes of ventricles or atria of small animals. The entire device is thin (thickness ~140 μm) and extremely lightweight (~16 mg).

[0096] One key feature of the MEA of the present disclosure is that it consists entirely of bioresorbable and biocompatible materials that eventually dissolve in the body. The microelectrodes 220 and interconnects 230 rely on Mo metal due to its relatively slow dissolution rate under physiological conditions, which could help to extend the device's operational lifetime compared to other metals such as magnesium. PLGA (lactide:glycolide 65:35) layer serves as the support layer 100 (thickness: 90 μm) for the MEA 225 and encapsulation layer 300 (thickness: 50 μm) to define microelectrode sizes. The fabrication process appears in FIG. 7 and is discussed in the Materials and Methods section below, which shows a high yield of 97% (n >40 MEA devices). In addition to the nanoscale patterns, the fabrication process for the bioresorbable transparent MEA is versatile and also compatible with the standard photolithography process, which can generate microscale grids with programmable parameters if needed (FIGS. 8A-8C).

[0097] The devices are bioresorbable transparent microelectrode arrays that allow multimodal investigation of the spatiotemporal cardiac characteristics to study and treat heart disease over clinically relevant temporary timescales and then fully dissolve inside the body without the need for additional surgical extraction. Our devices establish the foundations of a soft bioresorbable transparent MEA technology to greatly expand the landscape for bioresorbable transient electronics, with the potential to address the unmet needs in fundamental and translational cardiac research (e.g., ablation and surgical intervention procedures, postoperative recovery monitoring, post-infarction recovery, post-transcatheter aortic valve replacement (TAVR) recovery) where transient mapping and control of cardiac physiological parameters and functions are required. The devices represent the first optically transparent and bioresorbable microelectrode technology for cardiac applications. No devices with such capabilities exist before.

[0098] It is noted that the active layer 200 can be one or more conductors, such as electrodes 220. In certain embodiments, the active layer 200 can communicate by wire to an external

device, such as an external processing device. In other embodiments, the active layer can communicate wirelessly, such as by the active layer including a first coil and a second coil is placed external to the patient to perform wireless communication and/or inductive power transfer. In one embodiment, the active layer detects cardiac conditions and transmits detection signals with the detected information to the external processing device, which can then generate reports or data, including for example electronic and/or optical mapping. The present disclosure can conduct processing and mapping in any suitable manner, such as in U.S. Patent Publication Nos. 2018/0235692 and 2023/0085578, which are hereby incorporated by reference.

[0099] In one embodiment of the present disclosure, the external processing device can perform various functions and operations in accordance with the disclosure. The processing device can be, for instance, a computer, personal computer (PC), server or mainframe computer, or more generally a computing device, processor, application specific integrated circuits (ASIC), or controller. The processing device can execute software that can be stored on the storage device.

[00100] In one embodiment, the substrate layer 100 is a thin sheet. The substrate 100 is flat with a planar (though bendable) top surface and planar (though bendable) bottom surface (that faces and optionally touches the body (heart)). The active layer (e.g., nanogrid microelectrode array) 200 is placed over the substrate 100 and adhered to the top surface of the substrate 100 due to their high binding strength. The encapsulation layer 300 is then placed over the active layer and affixed to the substrate so that the encapsulation layer and substrate fully enclose the active layer sandwiched between the substrate layer and the encapsulation layer 300. The encapsulation layer 300 can have the same size and shape as the substrate layer 100. The substrate layer 100 and the encapsulation layer 300 can have a similar shape (or a different shape) as the active layer 200, and are larger than the active layer 200 to fully enclose the active layer 200 and so the combined substrate layer 100 and encapsulation layer 300 can be reliably affixed to the heart, such as by sutures. Or an adhesive can be placed on the bottom surface of the substrate layer 100. It is further noted that the period in which the bioresorbable materials dissolve can vary depending on the thickness of the materials.

[00101] The microelectrode arrays are transparent. This feature will allow photons to pass through both directions to allow direct observation of areas of interest under the microelectrode sites for concurrent optical diagnostics/therapies (e.g., endoscopy) and

guiding other procedures (e.g., catheters) on the hearts. It will also enable optical measurement of important cardiac parameters such as metabolic activity or intracellular calcium dynamics at locations underneath the microelectrodes using microscopes or cameras. The optical signals could be from intrinsic autofluorescent biomarkers in cells or external fluorescent indicators, which are not possible to measure electrically. Accordingly, for example, an optical layer can be placed over the device to transmit and receive optical signals to/from the patient's heart.

[00102] Meanwhile the microelectrode arrays provide electrical mapping of cardiac dynamics and on-demand electrical pacing to treat cardiac dysfunctions. Together, this will enable crosstalk-free and multiparametric investigation and treatment of heart diseases combining multiple modalities. The microelectrode arrays detect cardiac conditions and transmit those to a remote processing device for diagnostics and analysis, and also are used to apply a treatment pulse to the heart.

[00103] Bench testing of the 16-channel Mo nanogrid MEA

[00104] The physical and chemical properties of the Mo nanogrids could be adjusted by controlling nanogrid thickness and spacing. FIG. 1D presents the transmission spectra of Mo nanogrids (grid width: 500 nm, pitch: 6.75 μm) in the visible wavelength range at various thicknesses. As the nanogrid thickness increases from 100 to 500 and 1000 nm, the average transmittance value at 550 nm first decreases from 84.2 ± 1.0% to 80.0 ± 1.5% and then stabilizes at 79.1 ± 1.2%, respectively. FIG. 1E shows the effect of nanogrid pitch (grid width: 500 nm, thickness: 1000 nm) on optical transparency. As expected, the average 550 nm transmittance value increases from 53.5 ± 2.0% to 79.1 ± 1.2%, and 85.4 ± 1.1% when the pitch increases from 3.5 to 6.75, and 14.75 μm, respectively. Overall, the bioresorbable Mo nanogrid microelectrodes exhibit excellent optical transparency to allow light transmission in both directions.

[00105] Mo dissolves into nontoxic products in aqueous environments based on the reaction: $2Mo + 2H_2O + 3O_2 \rightarrow 2MoO_2^{2-} + 4H^+$. FIG. 1F demonstrates the dissolution kinetics and thickness profiles of the 1000 nm-thick Mo layers in 1× PBS (pH 7.4). The measured dissolution rate is 2.4, 19, and 62 nm/h at 37, 60 and 90 °C, respectively. At physiological temperature (37 °C), ~0.3 μg of Mo dissolves per day, which is within the safe daily intake (~45 μg). FIGS. 1G, 1H demonstrate the different dissolution stages of the MEA device immersed in 1× PBS (pH 7.4, 37 °C). The PLGA encapsulation and support layers

dissolve by hydrolysis into its monomers, lactic acid, and glycolic acid. The results show that the MEA completely dissolves after 25 weeks. SEM measurements further illustrate the changes in surface morphologies at different soaking periods, revealing that the Mo nanogrids on the PLGA substrate gradually develop cracks due to the swelling of the substrate induced by PLGA dissolution, and most of the nanogrid patterns disappear from the MEA region after 5 weeks (FIG. 9). High-resolution transmission electron microscopy (HRTEM) and energy dispersive X-ray spectroscopy (EDS) measurements (FIGS. 10A, 10B) show that the lattice structures of Mo remain unchanged at initial stages of soaking (the interplanar spacing is 0.21, 0.21, and 0.22 nm at Day 0, 1, and 2) while the oxygen content relative to Mo increases gradually in the devices.

[00106] Electrochemical impedance spectroscopy (EIS) and cyclic voltammetry (CV) measurements evaluate the recording and stimulation capability of the Mo nanogrid MEA. In general, a low impedance at the electrode/electrolyte interface helps the microelectrodes to suppress electrical noise and achieve high signal-to-noise ratios (SNRs) during recording. FIG. 2A displays the impedance curves of Mo nanogrid microelectrodes at various thicknesses (grid width: 500 nm, pitch: 6.75 μm). The 1 kHz impedance decreases from 44.2 ± 2.8 to 23.9 ± 0.9 and 13.8 ± 0.8 kilohms as the Mo nanogrid thickness increases from 100 to 500 and 1000 nm, respectively. FIG. 2B shows the impedance curves of the microelectrodes with various pitch values (grid width: 500 nm, thickness: 1000 nm). The 1 kHz impedance increases from 6.2 ± 0.4 to 13.8 ± 0.8 and 33.9 ± 1.5 kilohms as the pitch increases from 3.5 to 6.75, and 14.75 μm, respectively. FIG. 2C depicts the linear dependence of 1 kHz impedance on the microelectrode sizes from 500 × 500 to 100 × 100 μm^2, indicating the presence of a capacitive interface between the Mo nanogrid microelectrode and the electrolyte solution.

[00107] The phase angles of the microelectrode (-82.1° to -71.5°) at physiologically relevant low frequencies (10 Hz to 1 kHz) further confirm the capacitive electrode/electrolyte interface (FIG. 2D). Taking into account the balanced properties of optical transparency, electrochemical impedance, and device operational lifetime, the Mo nanogrid MEAs with a grid width of 500 nm, a pitch of 6.75 μm, and a thickness of 1000 nm are used in subsequent characterizations. FIG. 2E compares the normalized 1 kHz impedance of the microelectrodes to state-of-the-art non-bioresorbable transparent microelectrode material candidates with comparable optical transparency (~80%) for electrophysiological studies, including indium tin oxide (ITO), Au nanogrid, CNTs, graphene, and poly(3,4-

ethylenedioxythiophene):polystyrene sulfonate (PEDOT:PSS). The Mo nanogrid microelectrodes possess one of the most competitive electrochemical performances. FIG. 2F shows the CV curves of Mo nanogrid microelectrodes from -1.0 to -0.1 V at various scan rates from 20 to 200 mV/s. There is no observable distortion of the CV shape at a high scan rate of 200 mV/s, indicating the excellent electrochemical stability of the microelectrodes at high current densities, a feature desired for cardiac pacing. Cathodic charge storage capacity (CSC_c) is an important metric to quantify the electrical stimulation performance of the microelectrodes. The average CSC_c value of the Mo nanogrid microelectrodes is 9.52 ± 1.6 mC/cm^2, which is superior to many non-bioresorbable microelectrode materials, such as Pt, Au, titanium nitride, iridium oxide, graphene, CNTs, and ITO. See Table 1 below, which has a summary of CSC_c values for the Mo nanogrid microelectrodes and other reported electrode materials. See, J. Zhang, X. Liu, W. Xu, W. Luo, M. Li, F. Chu, L. Xu, A. Cao, J. Guan, S. Tang, X. Duan, Stretchable Transparent Electrode Arrays for Simultaneous Electrical and Optical Interrogation of Neural Circuits in Vivo. Nano Lett. 18, 2903-2911 (2018); W. Liu, M. W. Ashford, J. Chen, M. P. Watkins, T. A. Williams, S. A. Wickline, X. Yu, MR tagging demonstrates quantitative differences in regional ventricular wall motion in mice, rats, and men. Am. J. Physiol. Heart Circ. Physiol. 291, H2515-H2521 (2006); S.-K. Kang, S.-W. Hwang, S. Yu, J.-H. Seo, E. A. Corbin, J. Shin, D. S. Wie, R. Bashir, Z. Ma, J. A. Rogers, Biodegradable Thin Metal Foils and Spin-On Glass Materials for Transient Electronics. Adv. Funct. Mater. 25, 1789-1797 (2015); C. Li, C. Guo, V. Fitzpatrick, A. Ibrahim, M. J. Zwierstra, P. Hanna, A. Lechtig, A. Nazarian, S. J. Lin, D. L. Kaplan, Design of biodegradable, implantable devices towards clinical translation. Nat. Rev. Mater. 5, 61-81 (2020); P. Trumbo, A. A. Yates, S. Schlicker, M. Poos, Dietary Reference Intakes: Vitamin A, Vitamin K, Arsenic, Boron, Chromium, Copper, Iodine, Iron, Manganese, Molybdenum, Nickel, Silicon, Vanadium, and Zinc. J. Am. Diet. Assoc. 101, 294-301 (2001); and L. Lu, Recent Progress on Transparent Microelectrode-Based Soft Bioelectronic Devices for Neuroscience and Cardiac Research. ACS Appl. Bio Mater. 6, 1701-1719 (2023), the content of which are hereby incorporated by reference.

Electrode Materials	**CSC_c (mC/cm^2)**
Molybdenum nanogrids	9.52 ± 1.6
Platinum	3.6
Gold	0.3
Titanium nitride	2.47

Iridium oxide	11
Graphene	4.26 ± 1.6
CNTs	8.71 ± 3.3
ITO	0.058

TABLE 1

[00108] A high degree of uniformity in the electrochemical performance of an MEA is critical for high-fidelity electrical cardiac mapping and pacing. FIG. 2G presents the impedance responses of the 16 microelectrodes in a Mo nanogrid MEA, exhibiting an average 1 kHz impedance value of 14.2 ± 2.7 kilohms. The inset impedance colormap in FIG. 2G displays the spatial distribution of the 1 kHz impedance from the MEA to better visualize the uniform performance. FIG. 2H demonstrates the highly uniform CSC_c values of all 16 microelectrode channels. FIG. 2I shows that the MEAs maintain a stable electrochemical performance after 5000 bends against a small radius of 1 cm, suggesting the excellent mechanical compliance of the devices. The flexible mechanics is crucial to form a conformal contact with the curvilinear heart surfaces.

[00109] Recording 10 Hz sine waves at various physiologically related peak-to-peak amplitudes ranging from 100 μV to 20 mV in 1× PBS demonstrates the recording fidelity of the Mo nanogrid MEA (FIG. 3A and FIGS. 11A-11D). The 10 Hz impedance colormap and histogram of the MEA are shown in FIG. 12. No observable attenuation or distortion in the signal amplitude or morphology occurs, indicating the ability of the MEA to detect subtle electrophysiological signal changes. The power spectral density (PSD) results in FIG. 3B provide detailed frequency-domain information for the recorded signals. The large peak in the PSD curve corresponds to the 10 Hz input signal. The MEAs demonstrate highly uniform SNR and root mean square (RMS) noise, with an average SNR and RMS noise of 43.7 ± 1.7 dB and 36.3 ± 2.0 μV, respectively (FIGS. 3C, 3D). More SNR and RMS noise results from 64 other microelectrodes in 4 additional MEAs are available in FIGS. 13A-13H. Together, those measurements highlight the uniform performance for the microelectrodes both within the same MEA and across different MEAs in recording physiologically relevant signals.

[00110] Bioresorption behavior and its effect on the recording and stimulation properties of the MEA are critically important for temporary applications. Studies of the MEA performance changes during the resorption process are performed in 1× PBS at 37 °C. FIG. 3E presents average changes in the impedance (black line) and CSC_c (red line) from the microelectrodes over time. As expected, the impedance gradually increases, and CSC_c

gradually decreases due to the dissolution of Mo in PBS. The microelectrodes still exhibit moderate 1 kHz impedance (223.4 kilohms) and CSC_c (0.71 mC/cm^2) on Day 4.

[00111] Fitting the EIS results before and after resorption to an equivalent circuit model (FIG. 14) provides additional insights into the electrochemical behavior at the microelectrode-tissue interface. The model comprises solution resistance (R_s), the resistance of the oxide layer (R_{Oxide}), constant phase element (C_{PE}), charge-transfer resistance (R_{ct}) of the electrochemical corrosion process, and Warburg impedance (Z_w) for ion diffusion. A parallel capacitance (C_L) and resistance (R_L) are added in series to fit the impedance data at high-frequency domains due to the charge transfer process at the exterior surface of the microelectrode. The data from Day 0 and Day 4 closely match the fitting model (FIG. 3F). Table 2 below summarizes the fitting results, and shows fitted parameters of Mo nanogrid microelectrode EIS simulation. The increased R_s, R_L, R_{Oxide}, R_{ct} and Z_w on Day 4 suggest a rise in the overall resistance and ion diffusion pathways due to the Mo corrosion and dissolution at the electrode/electrolyte interface. Furthermore, C_{PE} is defined as $\frac{1}{Y_0(j\omega)^n}$, where Y_0, j, ω and n values represent the magnitude of C_{PE}, unit imaginary number, angular frequency, and a constant that determines the nature of the capacitance, respectively. The decrease in the n value (n value ranges from 0 to 1, where $n = 1$ represents an ideal capacitor and $n = 0$ represents a pure resistor) indicates a shift in the electrochemical behavior of the electrode surface from capacitive to more resistive, which aligns with the increase in overall resistance and correlates with the decrease in C_L.

Day		0	4
R_s (ohm)		5.85×10^{3}	1.64×10^{4}
R_L (ohm)		5.16×10^{3}	3.50×10^{4}
C_L (F)		2.57×10^{-7}	4.84×10^{-9}
R_{Oxide} (ohm)		2.30×10^{4}	1.57×10^{6}
R_{CT} (ohm)		206.1	1.88×10^{8}
C_{PE}	n	0.62	0.57
	Q (S×s^a)	3.47×10^{-7}	4.02×10^{-8}
Z_w (S×s$^{1/2}$)		3.26×10^{-7}	5.48×10^{-7}

TABLE 2

[00112] *Ex vivo* demonstration in various cardiac models

[00113] *Ex vivo* tests on rat hearts and human ventricular tissue slices demonstrate the functionalities and capabilities of the bioresorbable and transparent Mo nanogrid MEA for simultaneous, co-localized, electrical and optical interrogation of cardiac electromechanical function. FIG. 4A (top) illustrates the system for interfacing with rat hearts, where the MEA is attached to the left ventricle of a Langendorff-perfused heart for electrogram (EG) mapping, synchronized with a two complementary metal-oxide-semiconductor (CMOS) cameras-based optical mapping system for concurrent transmembrane potential (V_m) and intracellular calcium (Ca^{2+}) fluorescence mapping. The high transparency (between 77.6% and 80.3%) of the device from 520 to 780 nm enables efficient passage of the excitation and emission photons from the light source and voltage- and calcium-sensitive dyes (RH237 and Rhod-2 AM), allowing for multiparametric high-content assessment of cardiac tissue electrophysiological function from the same field of view (FIG. 4A bottom).

[00114] FIG. 4B demonstrates the time-aligned ECG reference (blue line) recorded by Ag/AgCl electrodes, EG signals from all 16 MEA channels (black lines), and simultaneous and co-localized V_m (red lines) and Ca^{2+} (purple lines) fluorescence signals from the area beneath each transparent microelectrode during sinus rhythm. The average heart rate recorded by the Mo nanogrid MEA EG results is 176 ± 1.1 beats per minute (BPM), which is consistent with that (176 ± 1.6 BPM) from the far-field ECG. No observable transients or oscillations occur in the recorded local field potentials (or spikes) from all MEA recorded EG traces, suggesting negligible light-induced artifacts during the light-emitting diode (LED) excitation illumination (520 nm, irradiance: 4.5 mW/mm^2) and fluorescence emission, consistent with the previous report.

[00115] Here, the Mo nanogrid MEA collects cardiac wave propagation profiles from the epicardium, while the voltage fluorescence signals present the dynamic V_m of cardiomyocytes located approximately 0.5-1 mm in depth of the cardiac tissue. The inward calcium channels open during the membrane depolarization allowing an influx of calcium ions into the cell. These calcium ions trigger the opening of the calcium-release channel of the sarcoplasmic reticulum membrane, resulting in the massive release of calcium into the cytosol to activate mechanical contractions. This process of calcium-induced calcium release causes a time delay between membrane depolarization and intracellular calcium transient, which is critically important in synchronizing cardiac contraction. The calculated EG-Ca^{2+} activation delay (5.49 ± 0.26 ms) matches well with the optical V_m-Ca^{2+} activation delay

(5.33 ± 0.87 ms), demonstrating the high-fidelity recording performance of the MEA to investigate cardiac excitation-contraction coupling.

[00116] FIG. 4C displays the electrical activation map (middle) constructed from the depolarization (activation) times of the MEA recorded EG signals, optical V_m (left) and Ca^{2+} (right) activation maps. All three maps are synchronized, with white squares highlighting the region covered by the transparent MEA. The total epicardial activation time obtained from the same region via the MEA and optical mapping is 1.6 and 1.5 ms, respectively. Here, the extracted apparent conduction velocity by the MEA is 257.7 cm/s during sinus rhythm. Apparent conductivity characterizes the propagation speed of depolarization waves from the epicardial surface, while the electrical waves originate from the sinoatrial node (e.g., sinus rhythm) and spread out through a complex three-dimensional architecture. The comparison between the EG, V_m, and Ca^{2+} activation maps visualizes the spatial-temporal distribution of the EG-Ca^{2+} and V_m-Ca^{2+} activation delays described previously. The high correlation between the EG and optical V_m maps of the same region further emphasizes the high-fidelity mapping capabilities of the MEA. The above results demonstrate that the Mo nanogrid MEA enables seamless interrogation of three notable cardiac parameters (EG, V_m and Ca^{2+}) via different imaging modalities to accurately detect cardiac wave propagation patterns as well as electrical and mechanical dynamics.

[00117] Moreover, the Mo nanogrid MEA is capable of electrical pacing using one or more microelectrodes in the array to modulate cardiac activity, treat abnormalities in the electromechanical properties, and simultaneously assess the pacing effects by electrical mapping using the rest microelectrodes. FIG. 4D demonstrates the EG, V_m, and Ca^{2+} activation maps upon electrical stimulation (400 BPM) delivered from the top right corner microelectrode in the MEA. Here, the extracted longitudinal (transverse) conduction velocities from the MEA and optical mapping during pacing are 56.9 (32.4) and 57.6 (32.6) cm/s, respectively. The three activation maps and their strong correlations (1) indicate successful capture of the heart rhythm, as the cardiac activation now originates from the pacing site and chronologically propagates throughout the heart surface in an anisotropic way; (2) highlight the synchronized cardiac pacing and high-fidelity mapping capabilities of the MEA. FIG. 4E summarizes representative QRS complexes recorded by the Mo nanogrid MEA across a relevant therapeutic period (Day 0 to Day 3) during sinus rhythm. As the device gradually dissolves in PBS, the amplitude of the recorded QRS complexes becomes

smaller. Gradually, the calculated SNR decreases from 35.7 ± 0.74 to 33.9 ± 0.68, 30.2 ± 0.71, and 26.8 ± 0.80 dB after 0, 1, 2, and 3 days in PBS, respectively.

[00118] *Ex vivo* demonstration on human ventricular slices (thickness: ~400 μm) validates the practical feasibility of the MEA in potential clinical scenarios (FIG. 4F). The high optical transparency of the MEA enables clear visualization of the underneath human cardiac tissue to facilitate device positioning. In FIG. 4G, the strong correlation between MEA EG and the optical V_m activation maps demonstrates the successful mapping of the electrical activities of human ventricular slices. The calculated conduction velocities in the tissue slice preparation from the MEA and optical mapping during pacing are both 24.5 cm/s, respectively. Taken together, the *ex vivo* results reveal that the bioresorbable and transparent Mo nanogrid MEAs are suitable for cross-platform cardiac electro/opto-physiological applications ranging from rat hearts to human cardiac tissue slices.

[00119] *In vivo* demonstration of AV block management

[00120] *In vivo*, open chest studies illustrate the performance of the Mo nanogrid MEAs in mapping and modulating the dynamic physiology of blood-perfused beating hearts. FIG. 5A displays the system, where the MEA is placed on the left ventricle of an actively contracting rat heart. FIG. 5B shows the cardiac wave propagation recorded by the MEA during sinus rhythm with an average heart rate of 378 ± 1.9 BPM, which is faster than the *ex vivo* rat heart excitation in FIG. 4C (177 ± 1.1 BPM) due to autonomic innervation of the cardiac conduction system and various circulating humoral factors and metabolic substrates absent from a Langendorff perfused heart. FIG. 5C show that the MEA can concurrently manipulate and map the cardiac wave propagation patterns from an *in situ* heart by unipolar pacing at 400 BPM (voltage: 2 V, pulse width: 2 ms) at different locations. In the unipolar pacing mode, one Mo nanogrid microelectrode functions as the cathode, and a remote Pt electrode works as the anode. Clinically, both unipolar and bipolar configurations are used in therapeutic pacing, while bipolar pacing is generally preferred because it requires a lower pacing threshold that consumes less energy, and minimizes pectoral muscle stimulation, which may occur during unipolar pacing due to current return to the pulse generator. FIG. 5D illustrates the control and capture of the cardiac excitation wave activation and propagation by bipolar pacing using the Mo nanogrid MEA (voltage: 1.5 V, pulse width: 2 ms), where two nearby microelectrodes in the MEA serve as the anode and cathode.

[00121] Cardiac pacing is frequently used in the clinic to treat abnormal heart rhythms such as bradycardia, where the heartbeat is too slow to support the normal cardiovascular

circulation. Bradycardia can be caused by several reasons, such as congenital heart defects, postsurgical complications, TAVR, and AV block. AV block is an interruption in transmitting an impulse between the atria and the ventricles, resulting in the desynchronization of atrial and ventricular excitation and a reduced heart rate. Ventricular pacing is widely used to re-synchronize ventricular and atrial contractions, restore normal heart rate and hemodynamics, and treat patients with AV block. FIG. 5E demonstrates the detection and treatment of AV block with the Mo nanogrid MEA. The ECG signals show a 3:1 AV block with ventricular contractions occurring at the slow rate of 58 BPM, indicated by three consecutive P waves and only one QRS complex. The ECG traces and EG signals recorded by the 14 sensing microelectrodes exhibit clear high-amplitude and wide QRS complexes during bipolar pacing at 400 BPM, showing the successful rhythm capture of the beating heart. Different shapes of the EG traces during bipolar pacing represent different depolarization and repolarization responses of the local cardiac tissue beneath each microelectrode.

[00122] The MEA maps different propagation patterns of the depolarization waves during AV block and pacing (FIG. 15). The measured longitudinal and transverse conduction velocities of the depolarization wave during MEA-initiated bipolar pacing are 51.1 and 31.6 cm/s, respectively. When the pacing stops, the AV block resumes with the rate of ventricular contractions of 55 BPM, indicating that the device pacing is responsible for and required to maintain a normal heart rate. FIG. 5F summarizes the QRS complexes recorded by the Mo nanogrid MEAs on Day 0, 1, 2, 3, 4 during sinus rhythm. The dissolution is completed in PBS while the EG mapping is performed on the blood-perfused beating hearts during *in vivo* open-chest measurements. The decline in SNR from the *in vivo* recording results is consistent with the *ex vivo* recording results in FIG. 4E, resulting from the increased impedance during the MEA dissolution process in PBS. It is important to note that the different features of the QRS complexes during sinus rhythm in FIG. 5F and FIG. 4E are normal and mainly determined by the locations of the microelectrodes on the heart and cardiac physiology since the EG results only represent electrical excitation of a local area under and near the microelectrodes instead of the whole heart in far-field ECG results. Similar differences exist in electrograms from non-bioresorbable Au microelectrodes (FIGS. 16A-16D) and are reported by other groups. These results demonstrate that the bioresorbable and transparent Mo nanogrid MEAs enable *in vivo* arrhythmias detection, monitoring, and treatment in the beating hearts for cardiac rhythm management.

[00123] *In vivo* bioresorbability and biocompatibility

[00124] The *in vivo* bioresorption process and biocompatibility of the Mo nanogrid MEAs are investigated by performing visual, functional, histological, and serological evaluations at different time points post MEA implantation. Rats of both sexes are randomly assigned into three groups (n = 3 animals per group): the control group does not receive any artificial interventions; the MEA group undergoes the open-chest surgery and MEA implantation via suture stitching of the device onto the left ventricular epicardium; the sham group undergoes the same open-chest surgery and suture stitching but without MEA implantation. The sham group at 2-weeks post sham surgeries and the MEA group at 2- and 6-weeks post-implantation surgeries are examined for visual traces of the MEA bioresorption. FIG. 6A displays the optical images of the hearts *in situ* (square box) and after explantation (circular box). The optical image at Week 0 shows that the MEA is mechanically robust to survive the surgical handling during implantation. At Week 2, the MEA partially dissolves with visible Mo pattern residues. At Week 6, the MEA completely disappears from the heart surface at the implantation region. Fibrotic tissues and non-bioresorbable prolene sutures exist in all rats of the MEA and sham groups, resulting in tissue damage during surgeries (e.g., stitching the epicardium).

[00125] FIG. 6B demonstrates the representative histology images of Masson's trichrome staining of cardiac tissues undergoing MEA implantation surgeries, where the red color represents muscle fiber (*i.e.*, cardiomyocytes) staining, the blue color represents collagen (*i.e.*, fibrotic area) staining, and the white color represents interstitial space. The green triangle indicates the epicardial side. Fibrosis occurs over the epicardial region where the MEAs are implanted. The normal myocardium comprises several major cell types (e.g., cardiomyocytes, fibroblasts, neurons, endothelial cells, etc.), forming a complex three-dimensional architectural network including the collagen scaffold and interstitial space. Pathophysiological conditions (e.g., cardiac injury, infarction, heart failure, infections) are characterized by myocardial fibrosis and interstitial space expansion, which, in turn, increase ventricular stiffness and lead to decreased electrical synchronization and mechanical contractility.

[00126] FIG. 6C exhibits the quantification of the histology examination, where the percentage volume of cardiomyocytes, fibrosis, and interstitial space reveals no statistically significant difference among all the groups ($P < 0.05$), which indicates negligible effects on the myocardial structures upon the MEA implantation and bioresorption. FIG. 6D depicts the

transthoracic echocardiogram test on the contractile function of the heart at different time points after implantation. Stroke volume and ejection fraction represent the volume and percentage of oxygen-rich blood pumped out from the left ventricle during each systolic contraction. A very low ejection fraction indicates impaired pumping action of the heart, which affects normal hemodynamics and is a hallmark of heart failure. Our results show no statistically significant difference in cardiac ejection fraction or volume among all the groups ($P < 0.05$), indicating no effect of our devices on normal contractility. The analysis of other hemodynamic parameters (*i.e.*, diastolic and systolic volume and diameter, cardiac output, and fractional shortening) shows similar normal results among different groups (FIGS. 17A-17F), indicating negligible effects on the mechanical function of the heart after the MEA implantation. FIG. 6E demonstrates the weights of the animals at different time points after implantation. An anticipated weight loss immediately after surgery is followed by a normal, gradual weight gain with age.

[00127] The serology tests (*i.e.*. complete blood count and blood chemistry) provide a comprehensive understanding of the health status of animals at different stages post-surgery (FIGS. 6F-6J and FIGS. 18A, 18B, 19A-19D). The blood levels of lipids, enzymes, metabolic wastes, immune cells, and electrolytes serve as indicators of organ-specific function and impairment as well as foreign body response upon the MEA implantation and bioresorption. Specifically, high cholesterol and triglycerides are associated with a higher risk of stroke or heart attack. Alkaline phosphatase reflects the function of liver to form and release bile while elevated alanine aminotransferase indicates potential hepatocellular injury. High creatinine and urea nitrogen levels indicate potential impaired renal function to excrete waste products and toxins. White blood cells (including lymphocytes, eosinophils, monocytes, and basophils) play critical roles in inflammatory reactions. Electrolytes can affect heart rate and rhythm, stabilize blood pressure, and support nerve and muscle function. The results (FIGS. 6F-6J and FIGS. 18, 19) show no statistically significant difference in organ function or physiological status among all the groups. The similar levels of average counts of red blood cells, white blood cells, monocytes, and lymphocytes indicate no notable inflammation in sham and MEA groups. The stable level of electrolytes shows the overall good health of animals in different groups. Together, those results suggest the harmless *in vivo* bioresorption of the Mo nanogrid MEA without abnormalities in the normal physiology of animals.

[00128] Discussion

[00129] The materials, device designs, and fabrication approaches reported here yield a fully bioresorbable and transparent MEA system that (1) provides mechanically compliant bidirectional electrical mapping and pacing over clinically relevant temporary timescales; (2) enables co-localized crosstalk-free multiparametric monitoring of cardiac behaviors. The MEA is lightweight, thin, highly transparent, possesses excellent mechanical flexibility, superior and uniform electrochemical performances, and complements those of the traditional non-bioresorbable MEAs. Studies on small animals and human hearts highlight the function of the MEA for spatiotemporal mapping of a list of critical cardiac parameters and demand-based site-specific unipolar and bipolar pacing to treat AV block.

[00130] Systematic bioresorption and biocompatibility evaluations demonstrate that the entire MEA has excellent biocompatibility and can fully dissolve from the implantation region in living animal models after 6 weeks, eliminating the need for secondary surgical procedures for device extraction. These concepts establish unique approaches in bioresorbable device technologies for fundamental studies of the pathophysiology of heart disease, with additional possible utility in developing effective clinical therapies, guiding surgical procedures, and monitoring postoperative recovery. Other embodiments include the development of wireless systems for power harvesting, control, and data communications, algorithms for automated closed-loop operations, optimization of the operational lifetimes to treat various forms of temporary heart conditions in clinical scenarios.

[00131] Materials and Methods

[00132] Fabrication of Mo nanogrid MEA

[00133] Referring to FIG. 7, the fabrication of the Mo nanogrid MEA 225 starts at step 1, with laminating an aluminum (Al) foil on a handling glass slide with polyimide tapes (e.g., Advanced Polymer Tape Inc.) on the edges. Oxygen plasma (50 W, 180 mTorr, 3 mins) is used to treat the prepared Al foil/glass slide before use. At step 2, Poly(methyl methacrylate) (PMMA) resist (MicroChem) was spin coated on the Al foil/glass slide and baked at 95 °C for 450 s. Electron beam (E-beam) evaporation deposited an 8 nm-thick Cr layer onto the PMMA layer to serve as a conductive layer for EBL. EBL defined the nanogrid MEA structure 225 via a beam current of 1 nA. Sputter deposition prepared a 1000 nm-thick Mo on the MEA followed by a lift-off process in acetone. Photolithography with AZ nLOF 2070 photoresist (Integrated Micro Materials) defined the interconnects 230 and bonding pad structures of the MEA. A second sputter deposition of Mo (1000 nm-thick) followed by lift-off in acetone completed the fabrication of the interconnects 230.

[00134] Afterwards, at step 3, a 25 wt% PLGA (65:35, Sigma-Aldrich Inc.)/ethyl acetate (anhydrous, 99.8%, Sigma-Aldrich Inc.) solution is spin coated onto the sample, followed by baking at 60 °C for 5 h and 110 °C for 2 h. Then, at step 4, the film is delaminated from the glass slide by gently peeling off the polyimide tapes on the edges without deforming the film. Finally, at step 5, immersing in hydrochloric acid (37%, High Purity Products) released the transparent Mo nanogrid MEA from the Al foil.

[00135] At step 6, the encapsulation PLGA layer 300 is prepared. A 15 wt% PLGA/ethyl acetate solution was spin coated on a soft lithography defined polydimethylsiloxane (PDMS) stamp, followed by baking at 60 °C for 2 h. After cooling down, the PLGA encapsulation layer 300 was gently peeled off from the PDMS stamp. The prepared PLGA encapsulation layer 300 and Mo nanogrid MEA 250 were then aligned together under a microscope, baked at 50 °C for 2 mins, and bonded in ethyl acetate vapor for 3 h. Finally, the device was baked at 50 °C for another 5 mins to improve the adhesion.

[00136] Optical, SEM, and mechanical measurements

[00137] A spectrophotometer (e.g., V-770 UV–vis/NIR, Jasco Inc.) measured the transmission spectra of the Mo nanogrid MEAs. SEM (e.g., PIONEER EBL, Raith Inc.) investigated the morphology of the nanogrids. A FEI Talos™ F200X scanning transmission electron microscope performed HRTEM and EDS measurements. A motorized test stand (e.g., ESM 1500, Mark-10) performed mechanical bending tests, in which the electrochemical performance was measured separately after a specific cycle of bending (FIGS. 20A, 20B).

[00138] Electrochemical measurements

[00139] EIS and CV measurements were conducted by a Gamry potentiostat (Reference 600+, Gamry Instruments Inc.) via a three-electrode configuration in 1× PBS (FIG. 21). In the configuration, an Ag/AgCl electrode, a Pt electrode, and the Mo nanogrid microelectrode served as the reference, counter, and working electrodes, respectively. CSC_c was calculated at a 50 mV/s scan rate. For benchtop measurement, a data acquisition system (e.g., PowerLab 16/35, ADInstruments Inc.) delivered 10 Hz sine wave signals with peak-to-peak amplitudes from 100 μV to 20 mV via a Pt electrode in 1× PBS. The microelectrodes in the Mo nanogrid MEAs detected the signals. The recorded signals were processed using MATLAB to obtain SNR and RMS noise.

[00140] Animals

[00141] All animal procedures were performed according to protocols approved by the Institutional Animal Care and Use Committee of The George Washington University and Northwestern University, and in conformance with the Guide for the Care and Use of Laboratory Animals published by the National Institutes of Health. Sprague-Dawley rats (Hilltop Lab Animals; male and female) at 10-17 weeks old were used.

[00142] Animal groups

[00143] Animals of both sexes were randomly assigned in three groups. Animals in the control group (n = 3) received no artificial procedures or interventions. Animals in the device group (n = 3) received the open-chest surgery and device implantation (including suture stitching of the device onto the epicardium). Animals in the sham group (n = 3) received the open-chest surgery and suture stitching without device implantation. We used non-resorbable sutures in order to indicate the location of devices after resorption.

[00144] Device implantation surgery and weight monitoring

[00145] The rat was anesthetized using isoflurane (1-3%). Once sedated, an intraperitoneal injection of buprenorphine (0.5-1.0 mg/kg) analgesia was administered. The rat was then placed supine on the intubation stage, and intubation was performed using the standard technique. Once intubated, the rat was placed on pressure control ventilation in the right lateral decubitus position. Animal ventilation was provided by the VentElite small animal ventilator (Harvard Apparatus, Holliston, MA). ECG leads were connected for intraoperative cardiac monitoring (lead II configuration). The left lateral chest was shaved and prepped using a sterile skin prep. The rat was then covered with a sterile drape, exposing the surgical site. The chest was palpated to identify the intercostal space where the point of maximum impulse could best be palpated. Scissors were used to make a curvilinear incision through the skin and subcutaneous tissue across the chest wall over the intercostal space. Metzenbaum scissors were then used to dissect through the chest wall muscles and into the thoracic cavity with care taken not to injure the lung. A rib spreader then opened the intercostal space. A cotton swab gently retracted the lung to expose the heart. Another cotton swab gently removed the pericardium. The MEA was then laid over the left ventricle. Two 6.0 prolene simple interrupted stitches (non-bioresorbable) secured the MEA to the heart. The cotton swab retracting the lung was carefully removed from the chest, and the lung was placed back over the heart on top of the device. The rib spreader was then removed, and the chest wall was closed with three single interrupted stitches using 4.0 polydioxanone (PDS)

sutures. The muscle layer was also closed using PDS with single interrupted sutures. The skin incision was closed with 4.0 nylon sutures in a running fashion. Anesthesia was then stopped, and the rat was allowed to recover on the ventilator until the point of self extubation. Appropriate postoperative monitoring and care were provided following surgery. The intraperitoneal dose of buprenorphine (0.5-1.0 mg/kg) analgesia was administered once every 12 h for 48 h following surgery. Animals (n = 3) were weighed every 4 days to monitor the weight post-surgery.

[00146] Echocardiogram

[00147] An echocardiogram was performed to evaluate the mechanical function of the left ventricle of the heart. n = 3 Sprague-Dawley rats for each group (*i.e.*, control, MEA implantation, sham). Control group did not receive any surgery and echocardiogram was performed directly. Echocardiogram of the MEA implantation group was performed at 2-, 4-, 6-, and 9-weeks post the implantation surgery. Echocardiogram of the sham group was performed at 2-weeks post the sham surgery. Rats were anesthetized by inhalation of 1-3% isoflurane vapors at 2 mL/min oxygen flow before and during the echocardiogram imaging with an EZ anesthesia machine (EZ Systems Inc., EZ-SA 800). Rats were transferred to the imaging stage after confirmation of loss of consciousness. Paws were affixed to the ECG electrodes (of the imaging stage) with electrode gel and tape to monitor the heart rate throughout echocardiogram imaging. Heart rate was maintained at 250-300 BPM. The left lateral chest was shaved, and ultrasound gel (Aquasonics) was applied to the skin. M-mode echocardiography of the left ventricle was performed using the Vevo 3100 system (VisualSonics/Fujifilm). The data were analyzed with VevoLAB2.1.0.

[00148] Lateral tail vein blood collection and serology test

[00149] n = 3 Sprague-Dawley rats for each group (*i.e.*, control, MEA implantation, sham). Control group did not receive any surgery and blood was collected directly. Blood from the MEA implantation group was collected at 2-, 4-, 6-, and 9-weeks post the implantation surgery. Blood from the sham group was collected at 2-weeks post the sham surgery. Blood was stored in (1) serum tubes (Sarstedt Inc., 1.3 mL micro tubes) for serum complete chemistry tests and (2) K3 EDTA tubes (Sarstedt Inc., 1.3 mL micro tubes) for complete blood count tests. A commercial company (Charles River Laboratories) conducted the assays.

[00150] Histology

[00151] n = 3 Sprague-Dawley rats for each group (*i.e.*, control, MEA implantation, sham). Control group did not receive any surgery and hearts were collected directly. Hearts from the MEA implantation group were collected at 2-, 4-, 6-, and 9-weeks post implantation surgery. Hearts from the sham group were collected at 2-weeks post the sham surgery. Rats were euthanized using 5% isoflurane vapors at 2 mL/min oxygen flow with an EZ anesthesia machine (EZ Systems Inc.) until loss of consciousness was confirmed via toe pinch. Hearts were excised and retrogradely perfused via an aortic cannula with cardioplegic solution (in mM, NaCl 110, KCl 16, $MgCl_2$ 16, $NaHCO_3$ 10, $CaCl_2$ 1.2, 4 °C) and then 10% neutral-buffered formalin. Hearts were transferred to a 70% ethanol solution after 24 hours of immersion (room temperature) in 10% neutral-buffered formalin. Cross sections of hearts were paraffin embedded, sectioned, and stained with Masson's trichrome for identification of myocardium (red color), fibrosis (blue color), and interstitial space (white color). Tissue samples were imaged using an EVOS XL light microscope (Thermo Fisher Scientific). A custom MATLAB code was used to quantify the percent volume of cardiomyocytes, fibrosis, and interstitial space in the images (*i.e.*, calculate the relative number of pixels per color in the selected region of interest).

[00152] Langendorff perfusion of the heart for *ex vivo* studies

[00153] Sprague-Dawley rats were anesthetized by ~3% isoflurane inhalation until no response to a toe pinch was confirmed. A cervical dislocation was performed followed by the thoracotomy. The heart was excised and retrogradely perfused via an aortic cannula in a constant pressure (70-90 mmHg) mode. A modified Tyrode's solution (in mM, NaCl 140, KCl 4.7, $MgCl_2$ 1.05, $CaCl_2$ 1.3, Glucose 11.1, HEPES 10, pH 7.4 at 37 °C) bubbled with 100% O_2 was used.

[00154] *Ex vivo* whole heart synchronized optical and electrical mapping

[00155] Optical mapping was performed as previously described. 10-15 μM blebbistatin (Cayman Chemicals, catalog number 13186) was added into the perfusion solution to suppress cardiac contractions. For optical mapping of V_m and calcium transients, the voltage-sensitive dye RH237 (1.25 mg/mL dye stock solution, Biotium, catalog number 61018) and calcium-sensitive dye Rhod-2 AM (1 mg/mL dye stock solution, Thermo Fisher Scientific, catalog number R1244) were added via bolus injection through the cannula. Fluorescence dyes were perfused for 15-20 mins (*i.e.*, equilibration period) before optical mapping studies to allow tissue staining and the washout of extra dyes. Excitation light at 520 ± 17 nm wavelength was used (LEX3-G Green LED System). V_m fluorescence was filtered

by a 695 nm long-pass filter and calcium fluorescence was filtered by a 572 ± 14 nm band-pass filter. Images of the front-lateral side of the left ventricle were captured at a speed of 2000 frames per second using two CMOS cameras (ULTIMA-L, SciMedia) with a 100 × 100-pixel resolution (15 × 15 mm^2 field of view). The MEA was placed on the front-lateral side of the left ventricle and connected to a data acquisition system (PowerLab 16/35, ADInstruments Inc.) with a sampling frequency of 20 kHz. Customized Pt bipolar electrodes or the Mo MEA were used to pace the heart from the left ventricle at rates higher than the intrinsic sinus rhythm of the heart. Electrical stimulation amplitude (*i.e.*, pacing voltage) was set at 2× the pacing threshold.

[00156] *Ex vivo* cardiac slice synchronized optical and electrical mapping

[00157] Tests with donor human ventricular tissue slices were approved by the Institutional Review Board at Northwestern University. Left ventricular slices were generated as previously described using a precision vibrating microtome in an ice-cold slicing solution (in mM, NaCl 140, KCl 6, $MgCl_2$ 1, $CaCl_2$ 1.8, glucose 10, HEPES 10, 2,3-butanedionemonoxime 10, pH 7.4 at 4 °C). The system is shown in FIG. 22. Slices were then allowed to recover at room temperature in a recovery solution (in mM, NaCl 140, KCl 4.5, $MgCl_2$ 1, $CaCl_2$ 1.8, glucose 10, HEPES 10, pH 7.4 at room temperature) for at least 20 mins before transferring to a bath at 37 °C and superfused with a modified Tyrode's solution (in mM, NaCl 128.2, $NaHCO_3$ 20, NaH_2PO_4 1.19, KCl 4.7, $MgCl_2$ 1.05, $CaCl_2$ 1.3, glucose 11.1, blebbistatin 10-15, pH 7.4 at 37 °C). After a 20 mins equilibration period, slices were stained with RH237 for voltage optical mapping. The MEA was positioned on the slice in the field of view of the camera. Slices were paced using a Pt bipolar electrode placed adjacent to the device at 1.5× amplitude of the threshold of stimulation. Optical traces were analyzed using a custom MATLAB software, Rhythm 3.0.

[00158] *In vivo* electrical mapping

[00159] Sprague-Dawley rats were anesthetized by 1-3% isoflurane inhalation until there was no response to a toe pinch. The rat was intubated and placed on pressure control ventilation in the right lateral decubitus position. Animal ventilation was provided by the VentElite small animal ventilator (Harvard Apparatus, Holliston, MA). ECG leads were connected for cardiac monitoring (lead II configuration), such as for example via the interconnect 230. The left lateral chest was shaved and palpated to identify the intercostal space where the point of maximum impulse could best be palpated. Scissors were used to make an incision through the skin and dissect the chest wall muscles to expose the thoracic

cavity with care taken not to injure the lung. A rib spreader was used to open the intercostal space. A cotton swab was used to gently retract the lung to expose the heart. Another cotton swab was used to gently remove the pericardium. AV block was induced as previously reported. Briefly, animals received (intraperitoneally, IP) 120 mg/kg caffeine (Millipore Sigma, catalog number C0750) and 60 mg/kg dobutamine (Cayman, catalog number 15582) sequentially. Fast pacing (cycle length 100 ms) was applied to the left ventricle for about 15 mins after drug treatment until an AV block was induced. The Mo nanogrid MEA was laid over the heart, covering the front-lateral side of the left ventricle. The MEA was connected to a data acquisition system (PowerLab 16/35, ADInstruments Inc.) with a sampling frequency of 20 kHz, such as for example via the interconnect 230. For cardiac pacing purposes, customized Pt bipolar electrodes or the MEA were used to pace the heart from the left ventricle at rates higher than the intrinsic sinus rhythm of the heart. Electrical stimulation amplitude (*i.e.*, pacing voltage) was set at 2× the pacing threshold. Rats were euthanized after tests. Cervical dislocation and heart extraction were performed after confirmation of no response to a toe pinch.

[00160] * * * *

[00161] It is noted that the drawings may illustrate, and the description and claims may use geometric or relational terms, such top, bottom, external, etc. These terms are not intended to limit the disclosure and, in general, are used for convenience to facilitate the description based on the examples shown in the figures. In addition, the geometric or relational terms may not be exact. For instance, walls may not be exactly perpendicular or parallel to one another because of, for example, roughness of surfaces, tolerances allowed in manufacturing, etc., but may still be considered to be perpendicular or parallel.

[00162] In addition, while the description indicates that certain materials are bioresorbable, they need not be 100% bioresorbable, but rather dissolve to a sufficient extent to pass safely from the body or otherwise avoid harm to the body so that they do not need to be manually removed from the body, and still be considered to be "bioresorbable" or "absorbable" within the spirit and scope of the present disclosure. And, the substrate layer 100, active layer 200, and encapsulation layer 300 need not be 100% transparent, but only sufficiently transparent to let light or signals pass through the respective layer.

[00163] The description and drawings of the present disclosure provided in the paper should be considered as illustrative only of the principles of the disclosure. The disclosure may be configured in a variety of ways and is not intended to be limited by the preferred

embodiment. Numerous applications of the disclosure will readily occur to those skilled in the art. Therefore, it is not desired to limit the disclosure to the specific examples disclosed or the exact construction and operation shown and described. Rather, all suitable modifications and equivalents may be resorted to, falling within the scope of the disclosure.

5

Claims

1. An optical cardiac device comprising:

a transparent flexible substrate layer, said substrate layer comprising a first bioresorbable material;

a transparent flexible active layer having one or more flexible conductors coupled to said substrate, wherein said active layer is configured to conduct diagnostic and therapeutic analysis and/or treatment of a patient's heart, said active layer comprising a second bioresorbable material; and

a transparent flexible encapsulation layer encapsulating said flexible active layer, said encapsulation layer comprising a third bioresorbable material.

2. The cardiac device of claim 1, wherein the first bioresorbable material is the same as the third bioresorbable material.

3. The cardiac device of claim 1 or 2, wherein said one or more flexible conductors comprise a microelectrode.

4. The cardiac device of any one of claims 1-3, wherein said cardiac device is configured to be coupled directly to a patient's heart.

5. The cardiac device of any one of claims 1-4, wherein said cardiac device is configured to be coupled to a patient's heart by suture and/or adhesive.

6. The cardiac device of any one of claims 1-5, wherein the first bioresorbable material, the second bioresorbable material, and the third bioresorbable material are configured to dissolve in the patient's body.

7. The cardiac device of any one of claims 1-6, wherein the first bioresorbable material, the second bioresorbable material, and the third bioresorbable material are configured to completely dissolve in the patient's body within a period of approximately 25 weeks.

8. The cardiac device of any one of claims 1-7, wherein the first bioresorbable material, the second bioresorbable material, and the third bioresorbable material are configured to mostly dissolve in the patient's body within a period of approximately 5-6 weeks.

9. The cardiac device of any one of claims 1-8, wherein the first bioresorbable material, the second bioresorbable material and the third bioresorbable material are configured to dissolve in the patient's body.

10. The cardiac device of any one of claims 1-9, wherein the first bioresorbable material comprises polylactic-co-glycolic acid, the second bioresorbable material comprises polylactic-co-glycolic acid, and the third bioresorbable material comprises molybdenum.

11. The cardiac device of any one of claims 1-10, wherein said one or more flexible conductors comprise an array.

12. The cardiac device of any one of claims 1-11, wherein said active layer provides electrical/optical mapping of cardiac dynamics including heart rhythm, biopotentials, oxygenation, metabolic state, calcium homeostasis, activation propagation pattern, and/or myocardial conduction and contraction.

13. The cardiac device of any one of claims 1-12, wherein said active layer provides on-demand site-specific pacing.

14. The cardiac device of any one of claims 1-13, wherein the first bioresorbable material, the second bioresorbable material and the third bioresorbable material are non-toxic.

15. The cardiac device of any one of claims 1-14, further comprising void spaces between said one or more conductors, said void spaces configured to allow photons to pass through said one or more conductors for optical operations, such as imaging of

autofluorescent biomarkers or other fluorescent indicators with microscopes and camera systems.

16. The cardiac device of any one of claims 1-15, whereby said first, second and third bioresorbable materials safely dissolve in the patient's body to a point that they pass safely from the patient's body or do not need to be manually removed from the patient's body.

17. An optical cardiac device comprising:

a transparent flexible substrate layer, said substrate layer comprising a first dissolvable material;

a transparent flexible active layer having one or more flexible conductors coupled to said substrate, wherein said active layer is configured to conduct diagnostic and therapeutic analysis and/or treatment of a patient's heart, said active layer comprising a second dissolvable material; and

a transparent flexible encapsulation layer encapsulating said flexible active layer, said encapsulation layer comprising a third dissolvable material.

18. The cardiac device of claim 17, whereby said first, second and third dissolvable materials safely dissolve in the patient's body to a point that they pass from the patient's body or do not need to be manually removed from the patient's body.

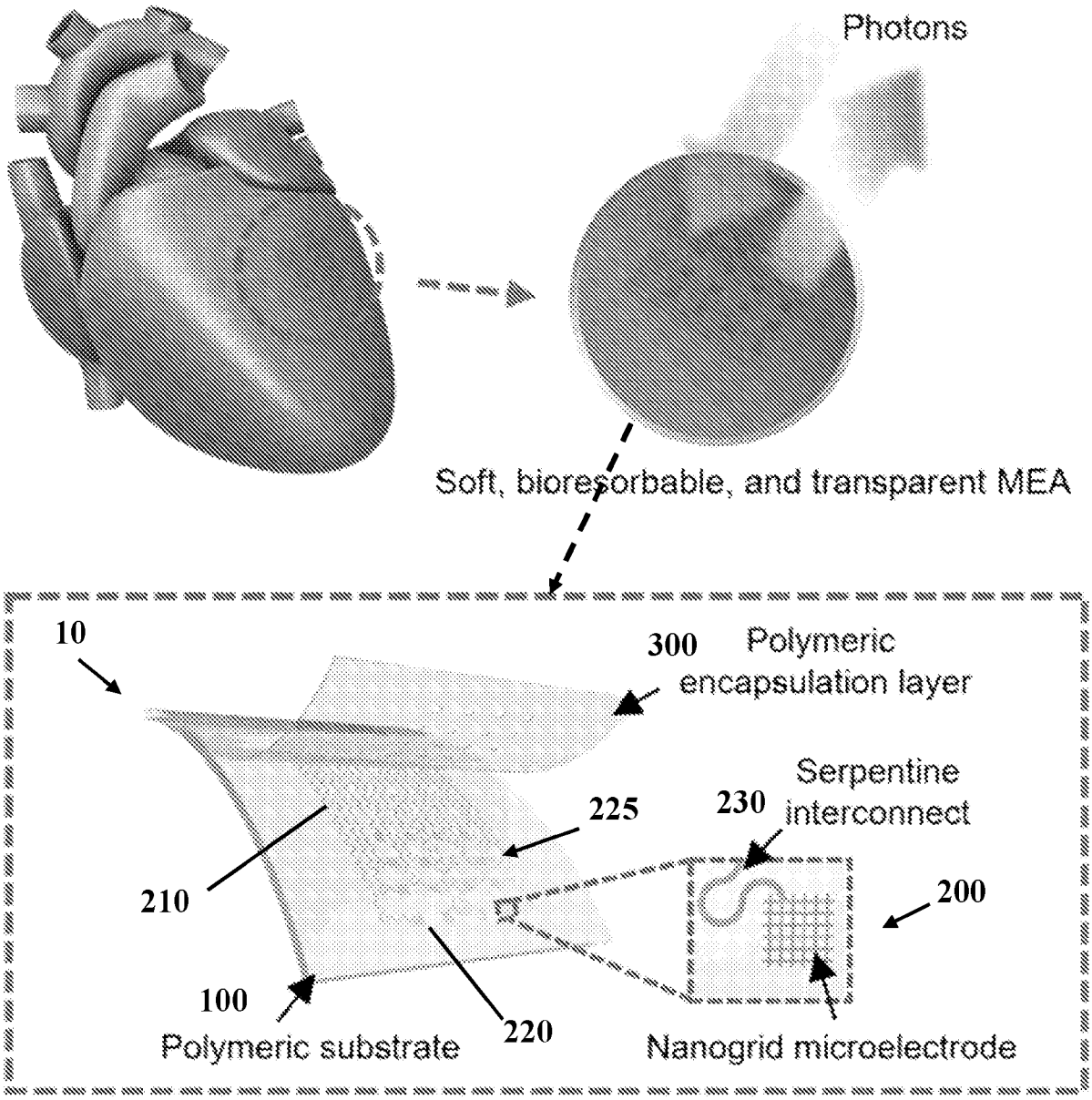

Photons
Soft, bioresorbable, and transparent MEA
10
300
Polymeric
encapsulation layer
Serpentine
interconnect
225
230
210
200
100
Polymeric substrate
220
Nanogrid microelectrode

FIGURE 1A

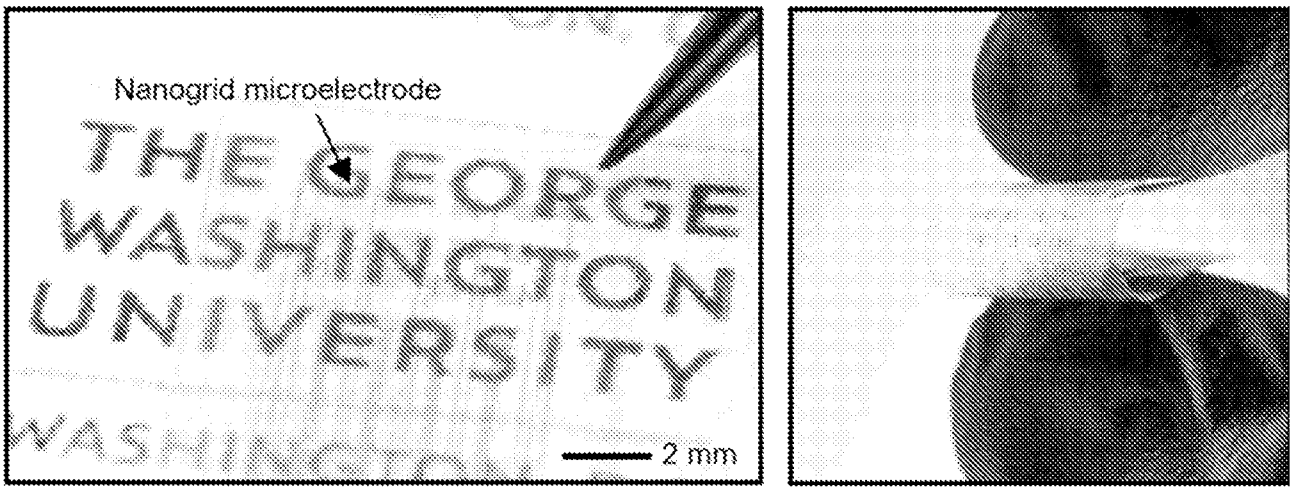


FIGURE 1B

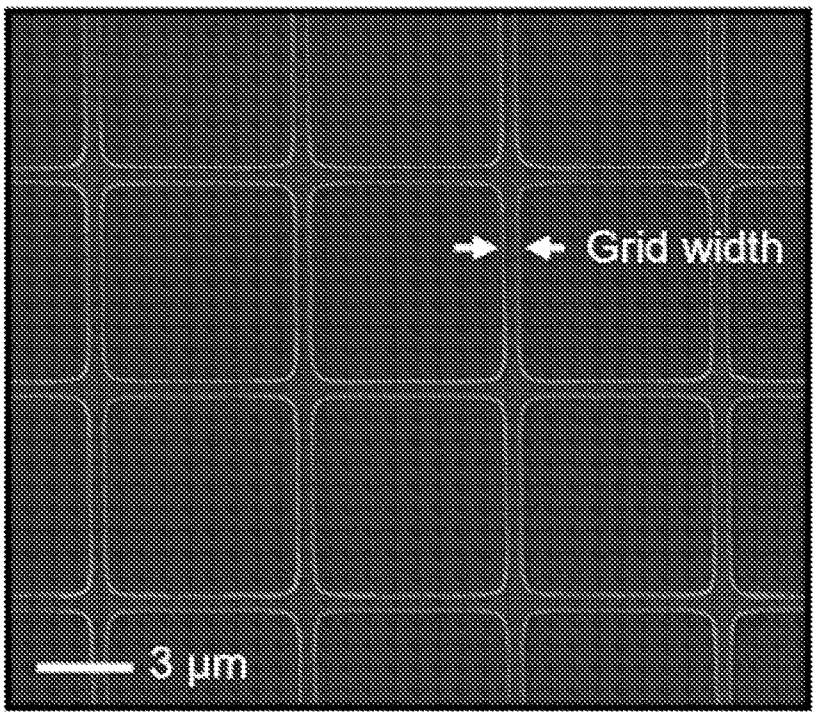


FIGURE 1C

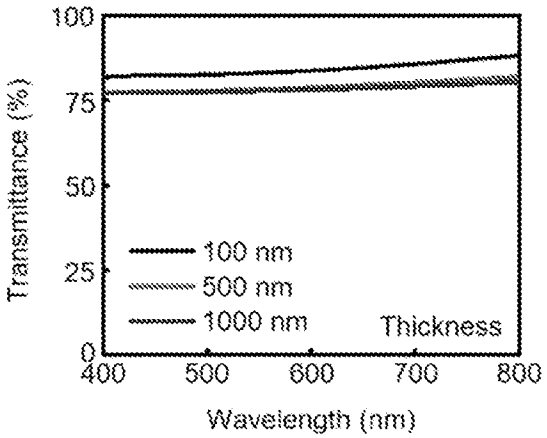


FIGURE 1D

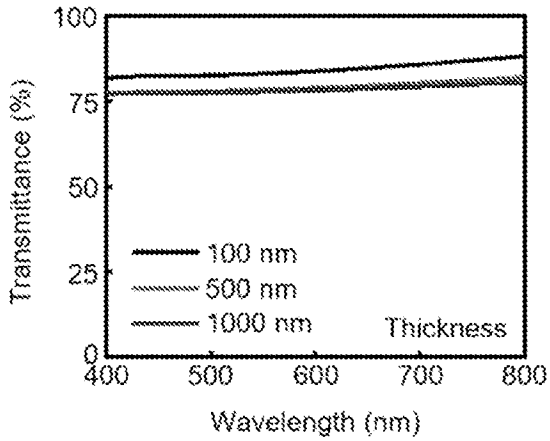


FIGURE 1E

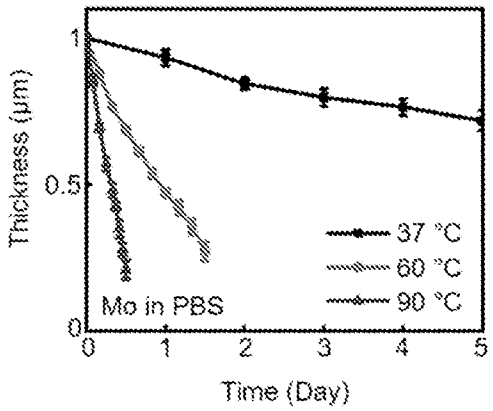


FIGURE 1F

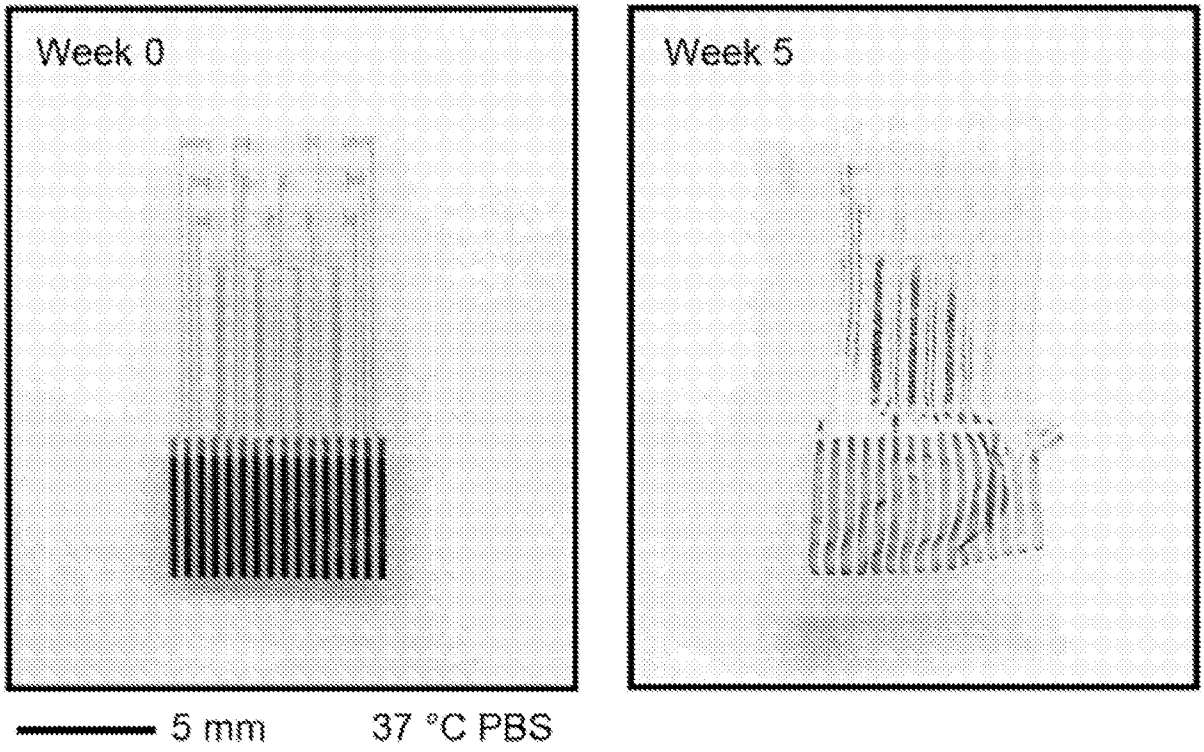


FIGURE 1G

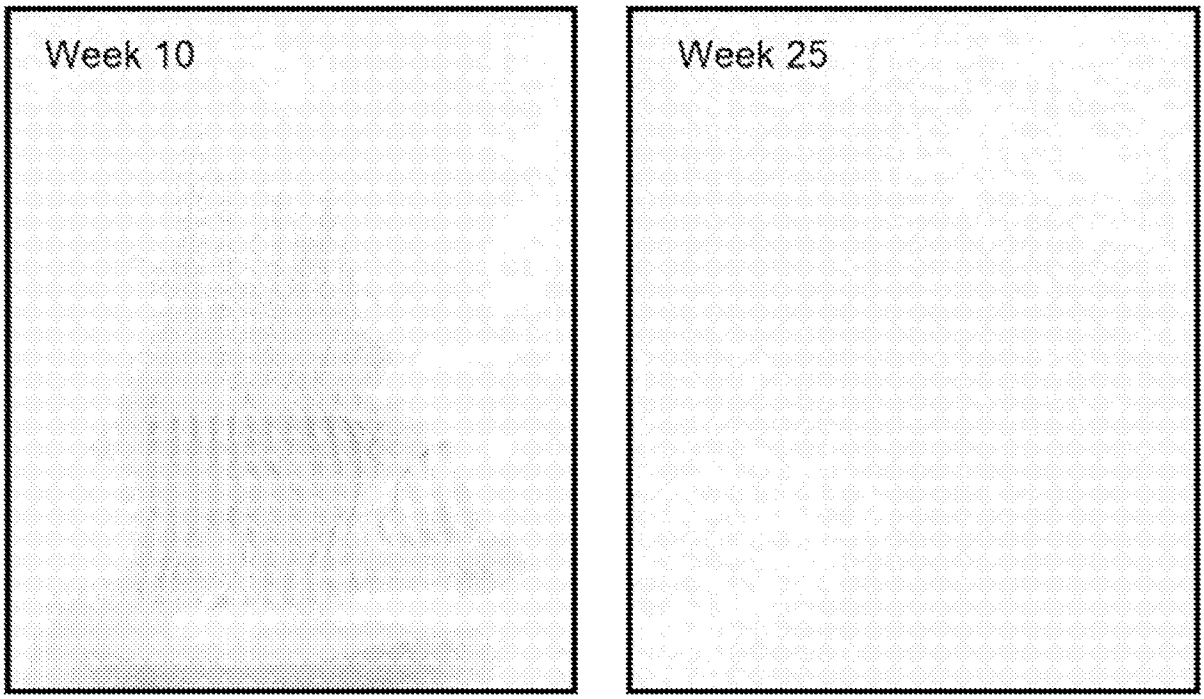


FIGURE 1H

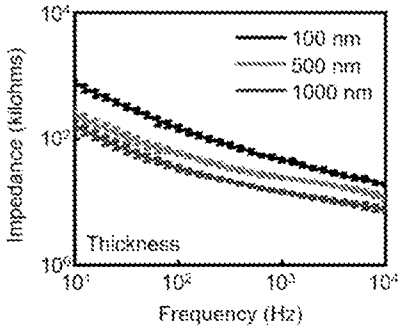


FIGURE 2A

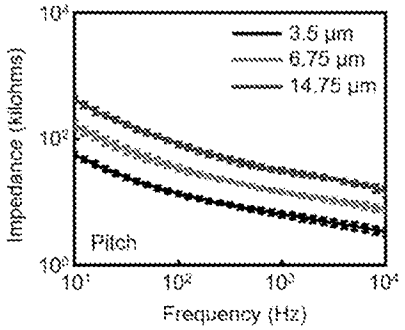


FIGURE 2B

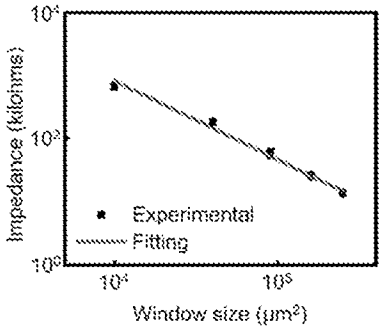


FIGURE 2C

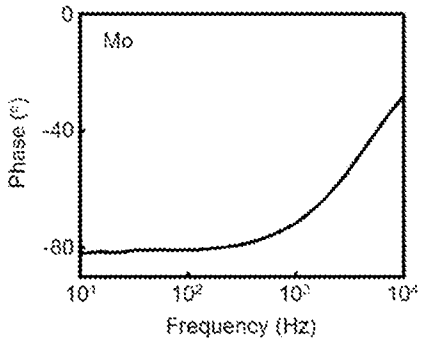


FIGURE 2D

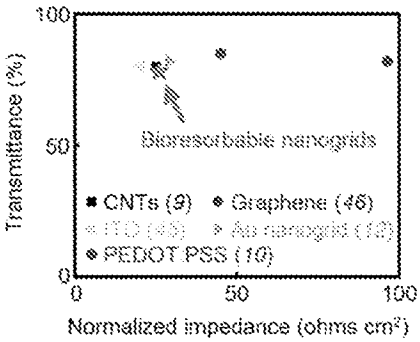


FIGURE 2E

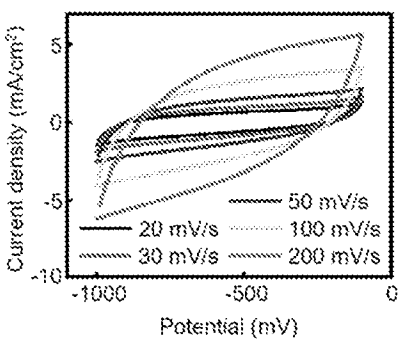


FIGURE 2F

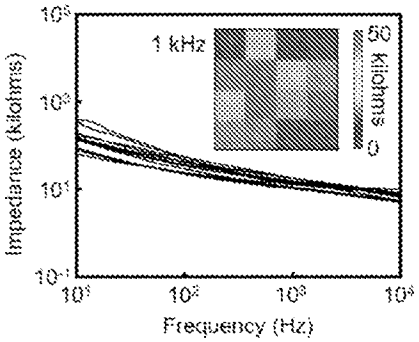


FIGURE 2G

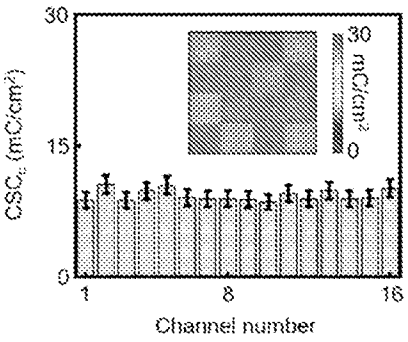


FIGURE 2H

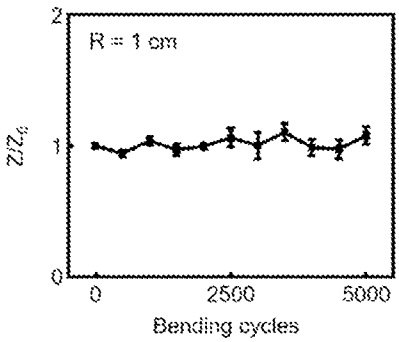


FIGURE 2I

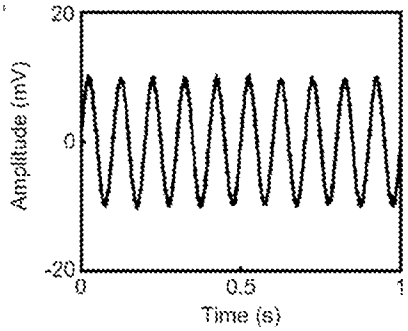


FIGURE 3A

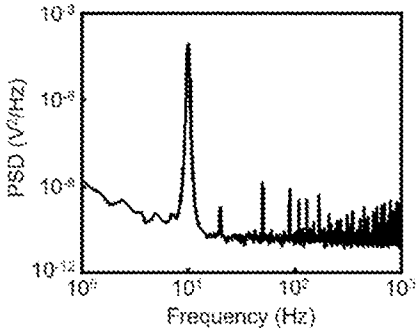


FIGURE 3B

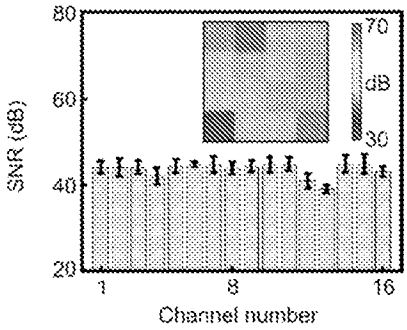


FIGURE 3C

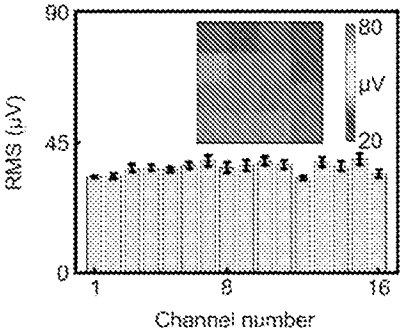


FIGURE 3D

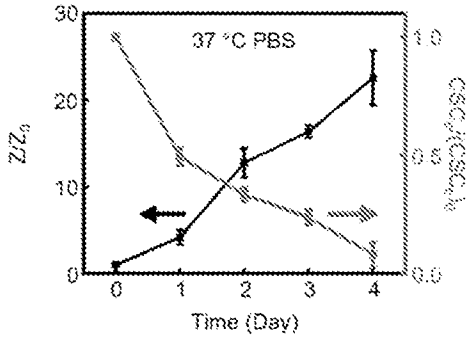


FIGURE 3E

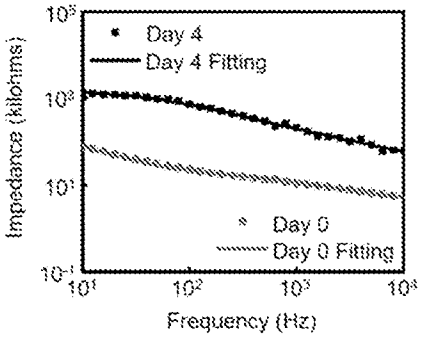


FIGURE 3F

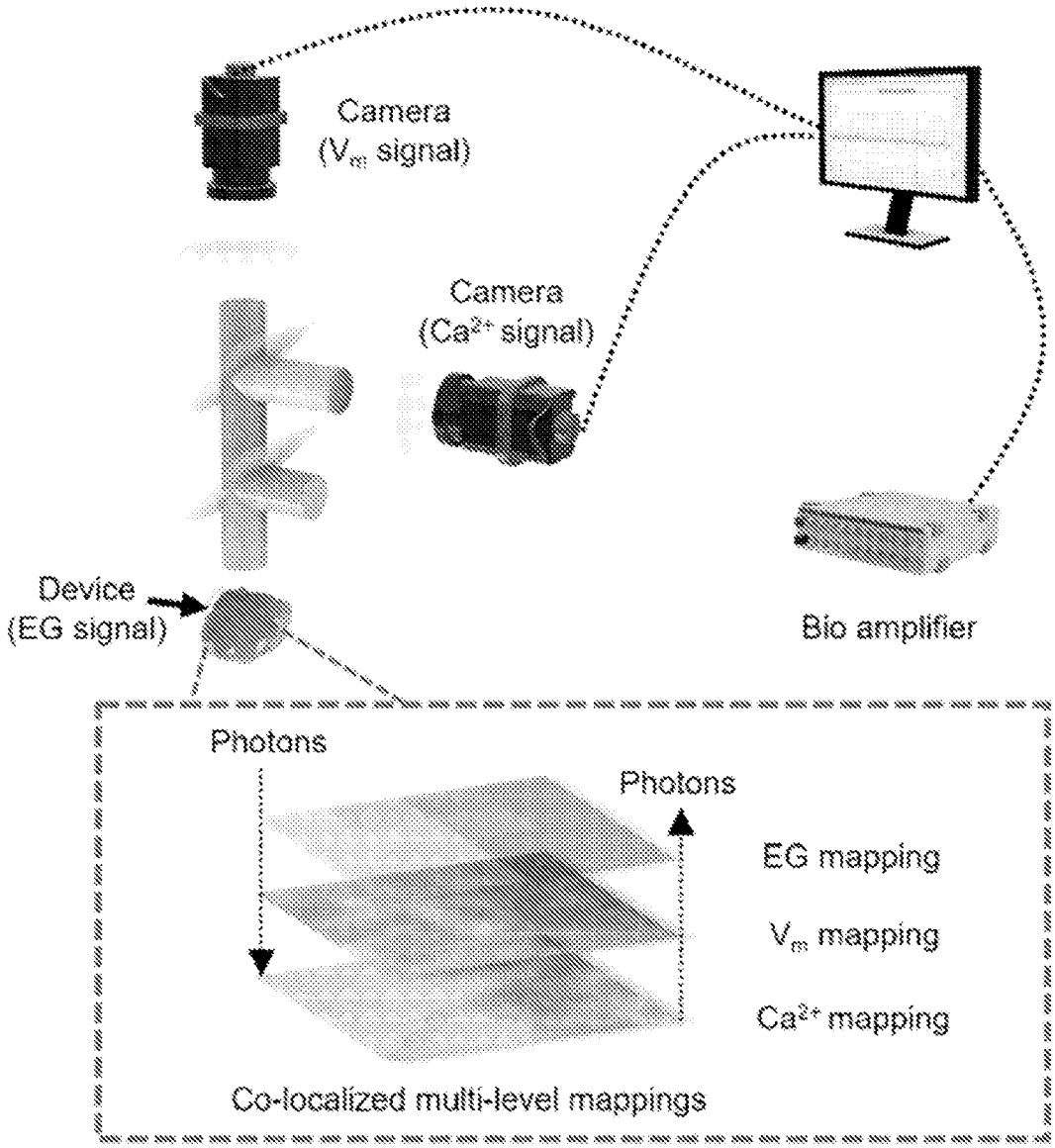

Camera
(V_m signal)
Camera
(Ca^{2+} signal)
Device
(EG signal)
Bio amplifier
Photons
Photons
EG mapping
V_m mapping
Ca^{2+} mapping
Co-localized multi-level mappings

FIGURE 4A

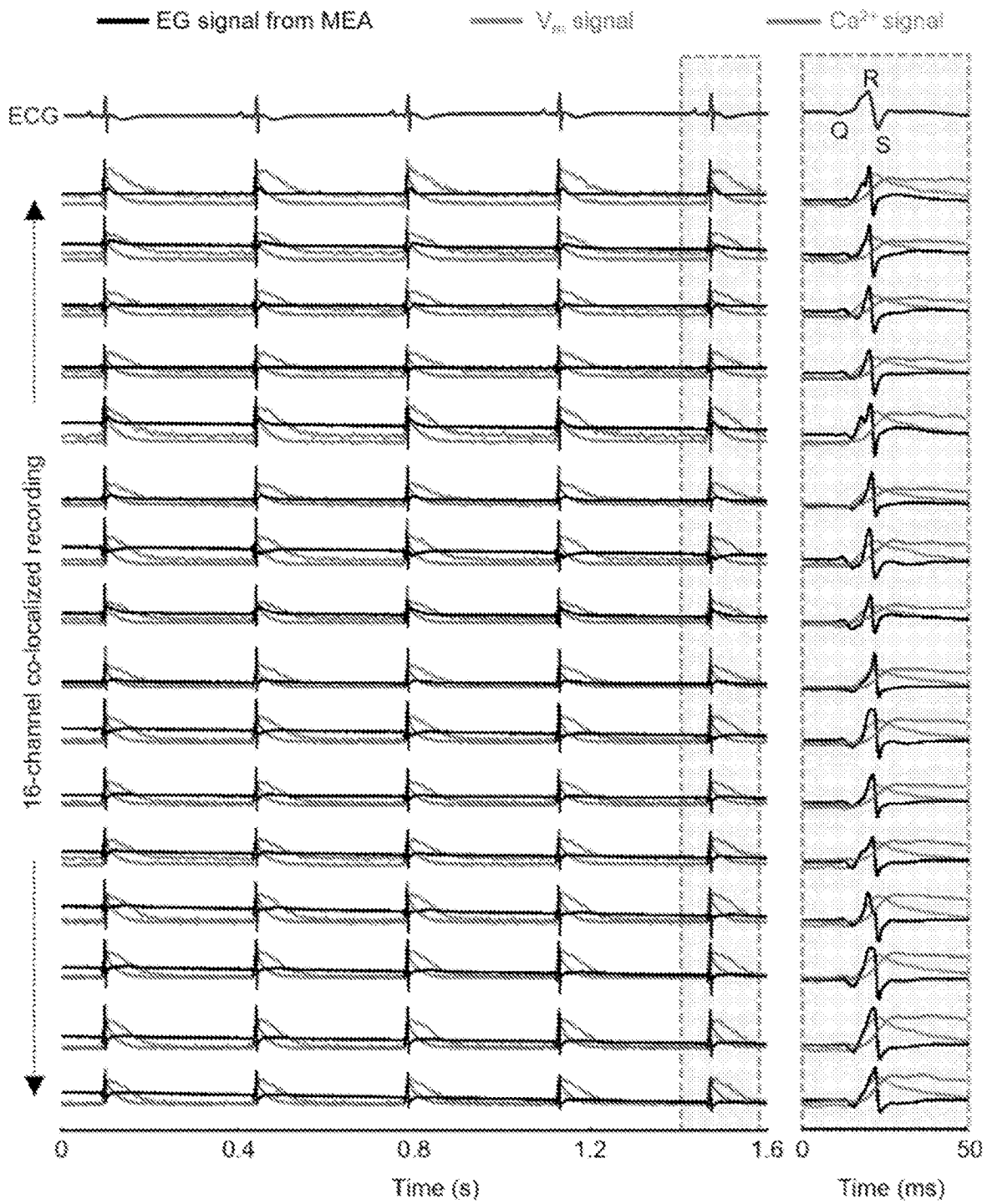

EG signal from MEA
V_m signal
Ca^{2+} signal
ECG
R
Q
S
16-channel co-localized recording
0
0.4
0.8
1.2
1.6
Time (s)
0
50
Time (ms)

FIGURE 4B

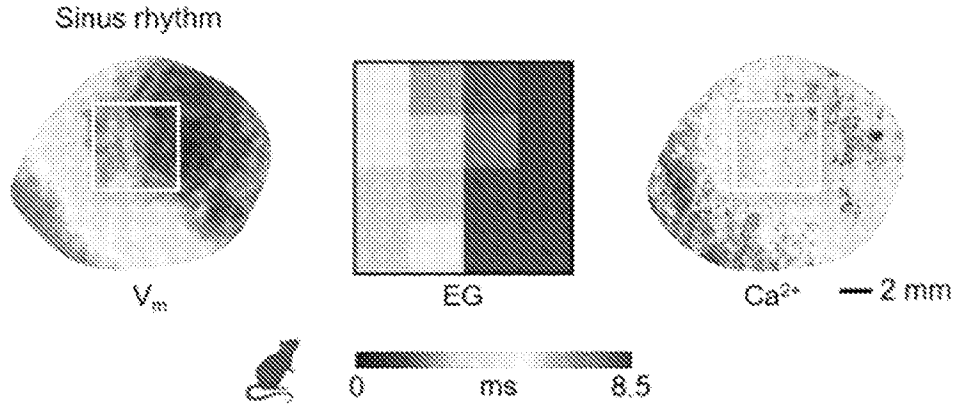


FIGURE 4C

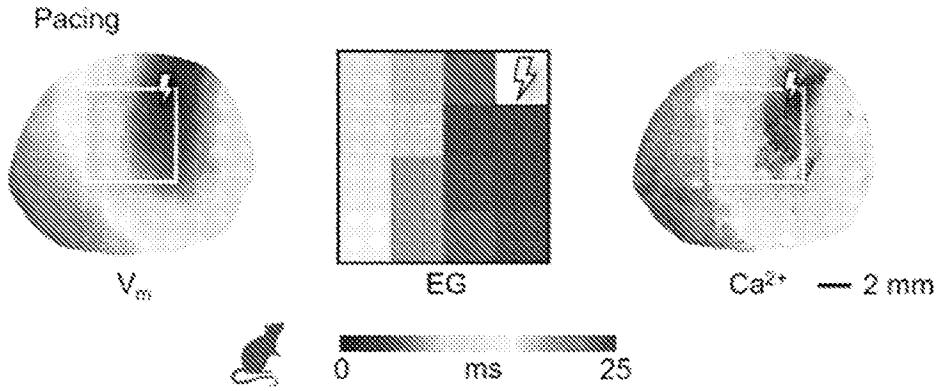


FIGURE 4D

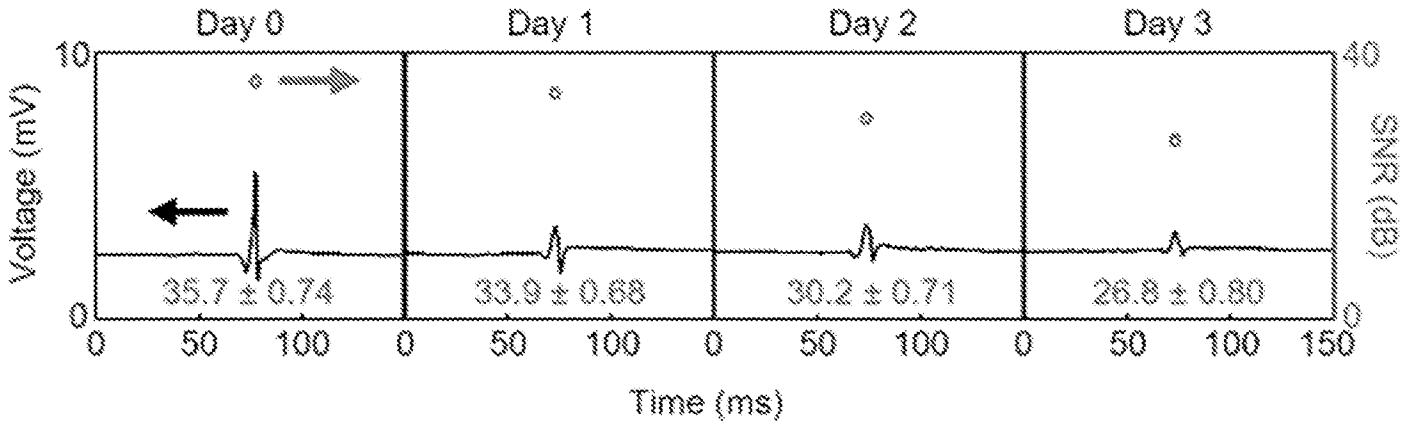


FIGURE 4E

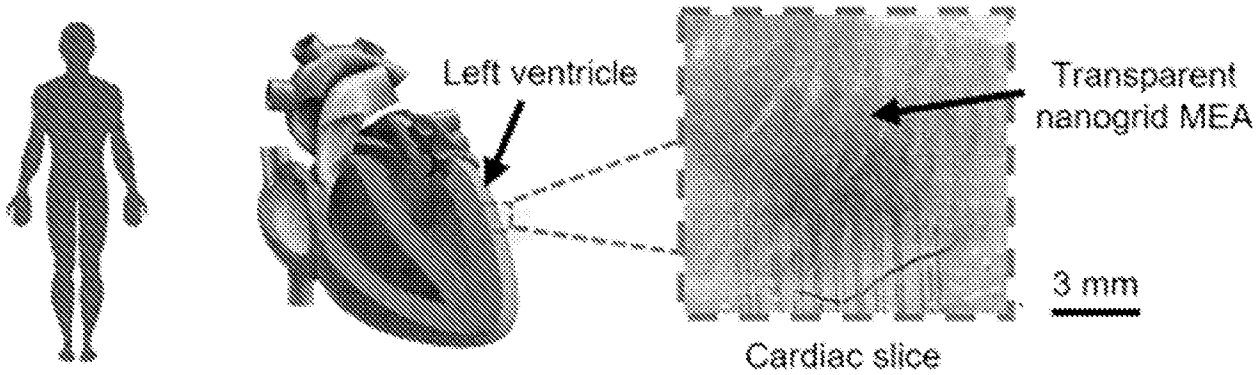


FIGURE 4F

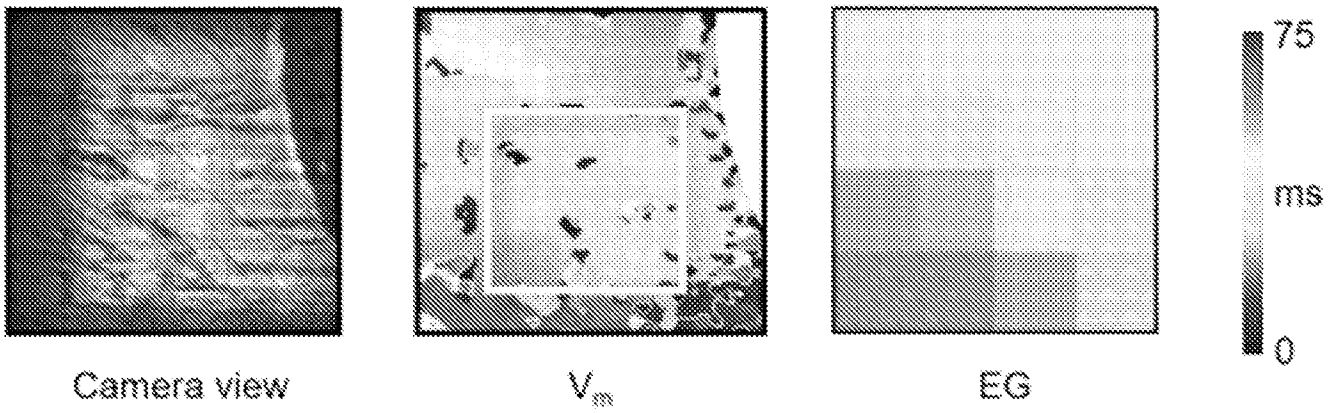


FIGURE 4G

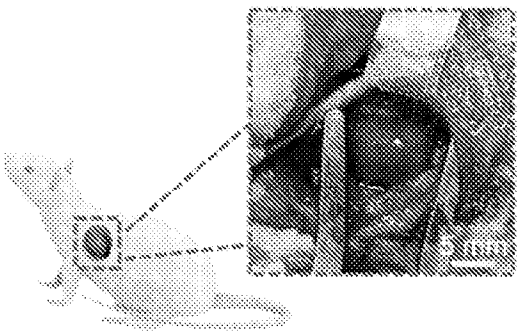


FIGURE 5A

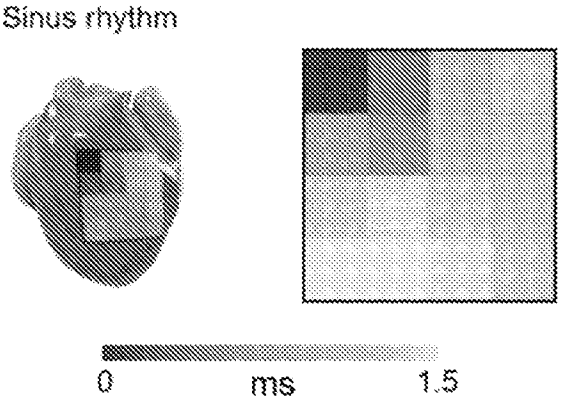


FIGURE 5B

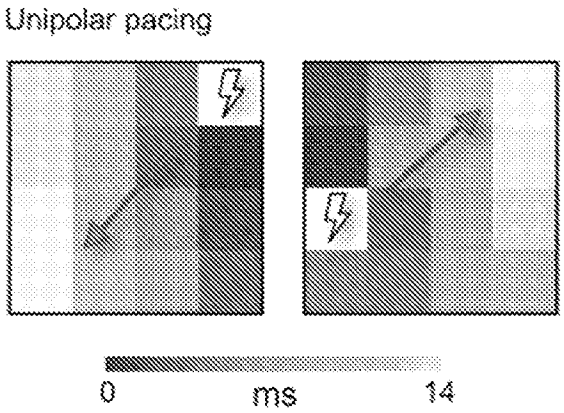


FIGURE 5C

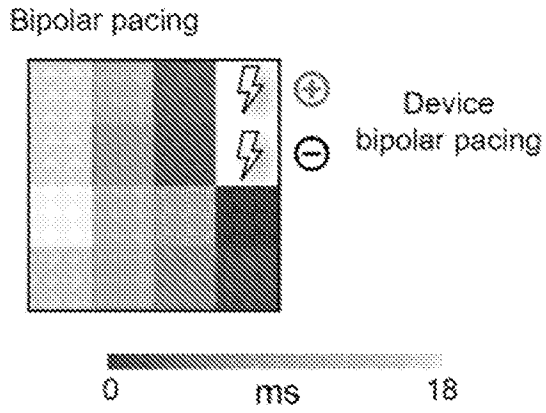


FIGURE 5D

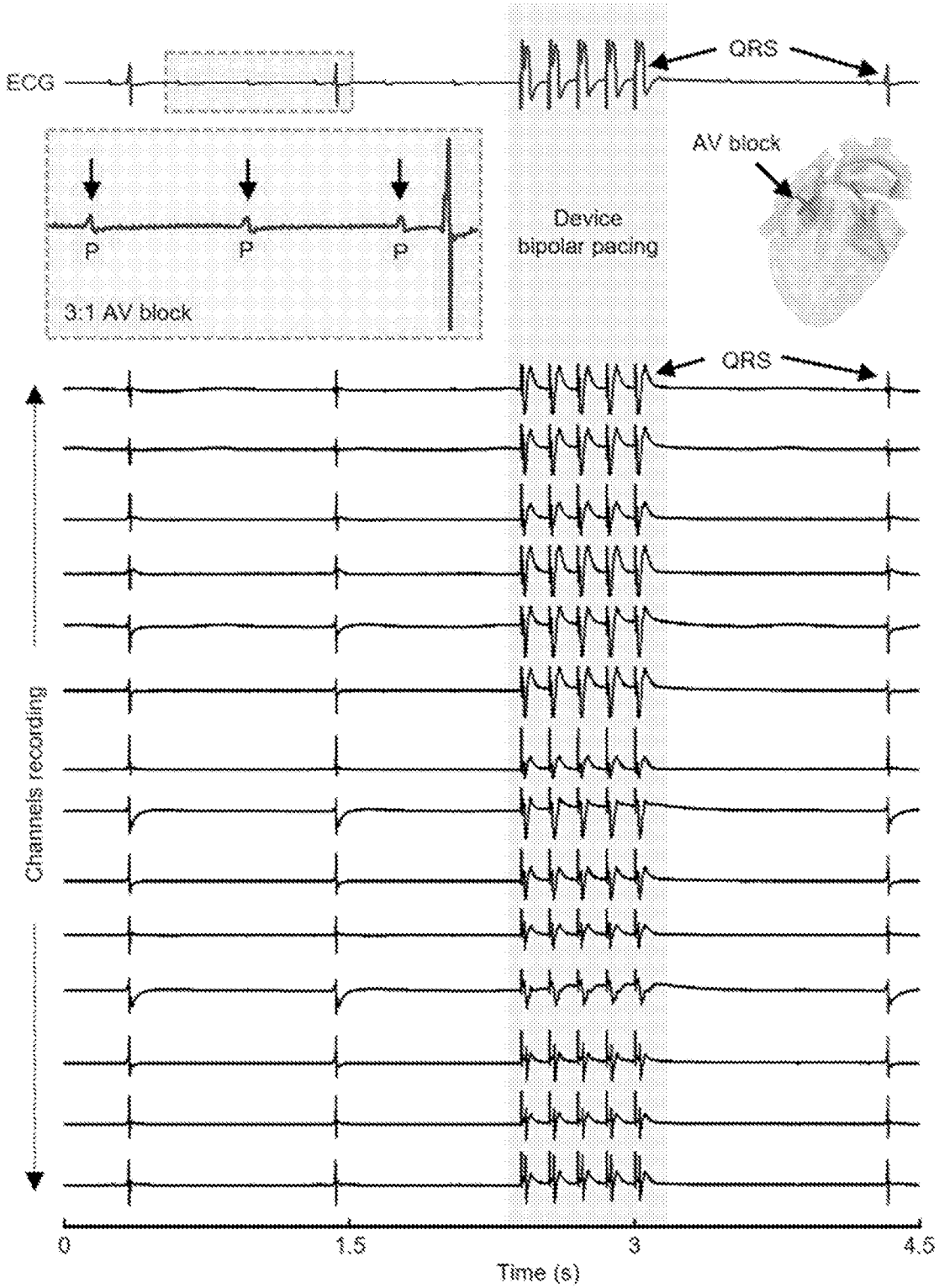

ECG
QRS
AV block
Device
bipolar pacing
P
P
P
3:1 AV block
QRS
Channels recording
0
1.5
3
4.5
Time (s)

FIGURE 5E

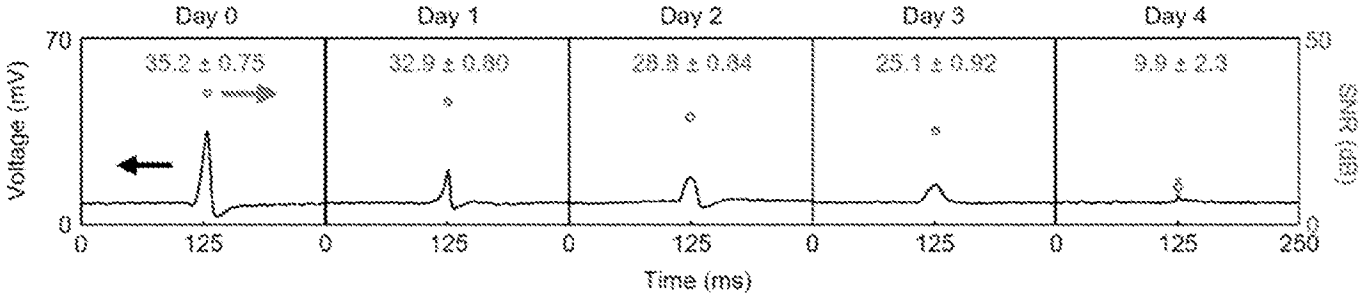


FIGURE 5F

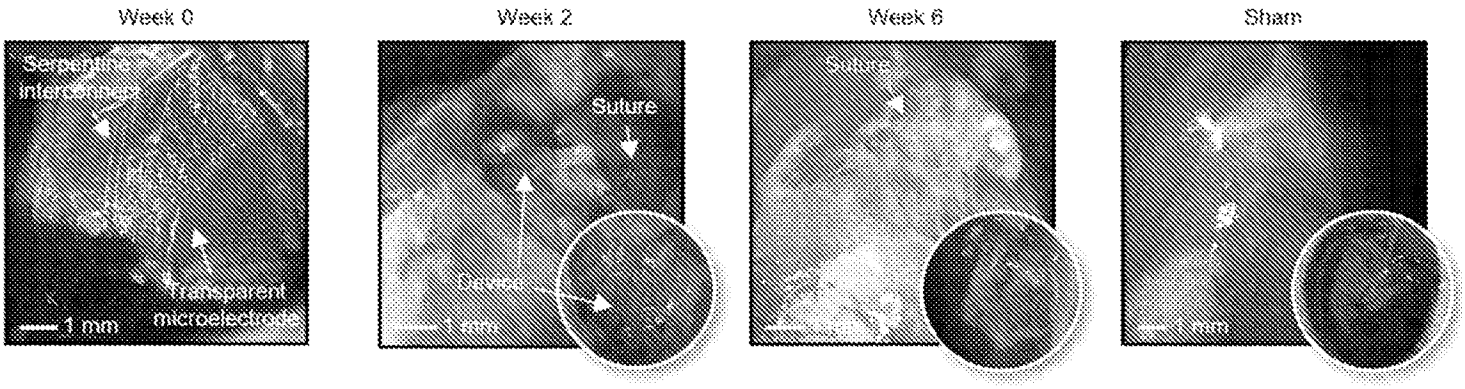


FIGURE 6A

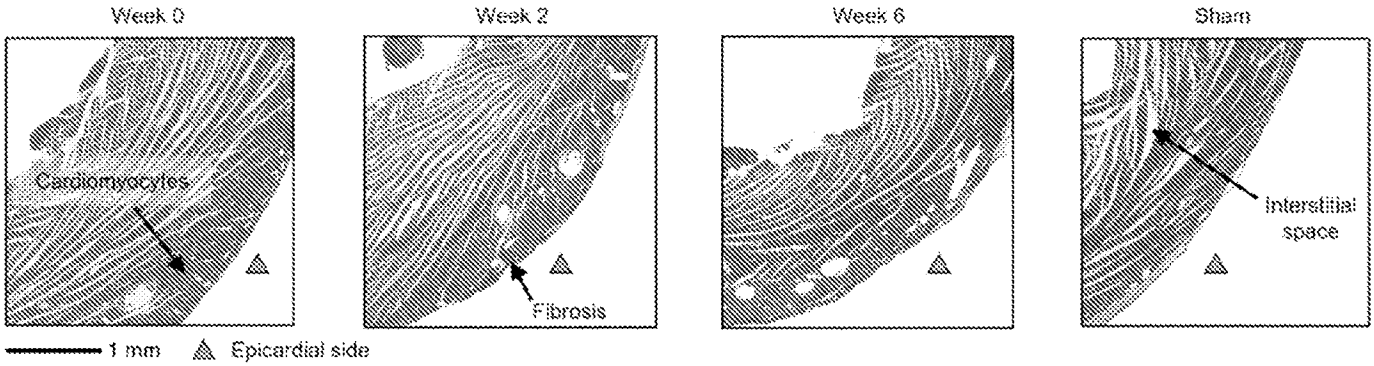


FIGURE 6B

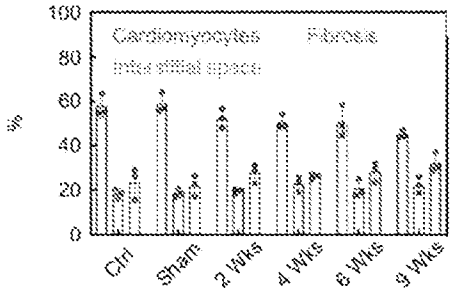


FIGURE 6C

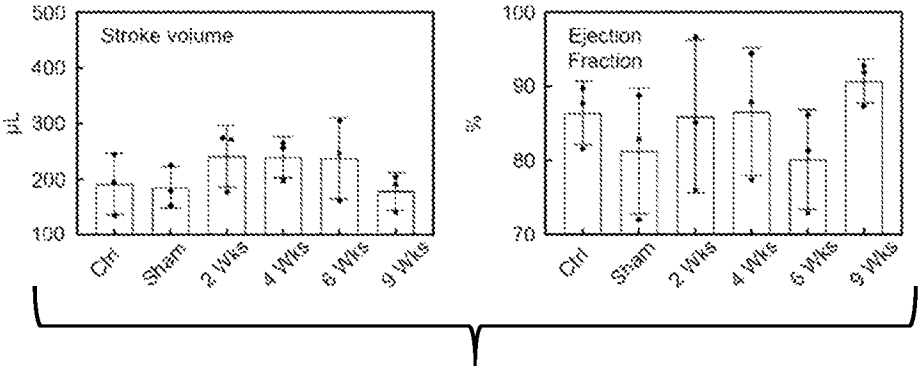


FIGURE 6D

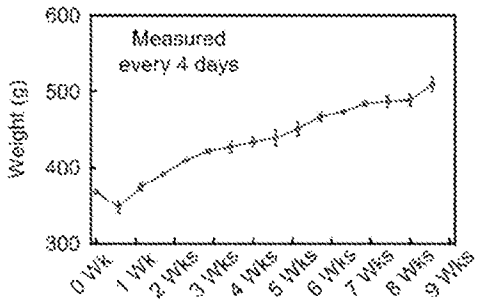


FIGURE 6E

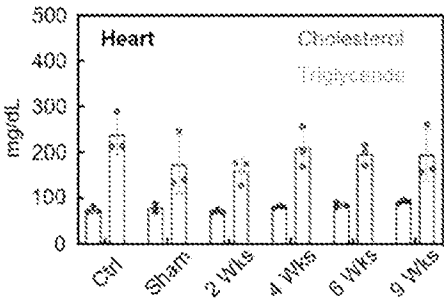


FIGURE 6F

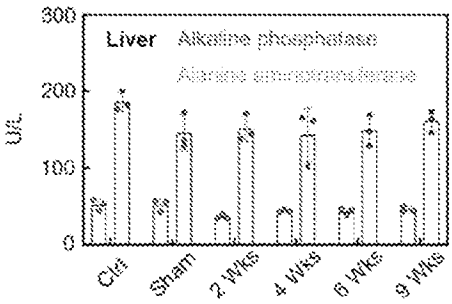


FIGURE 6G

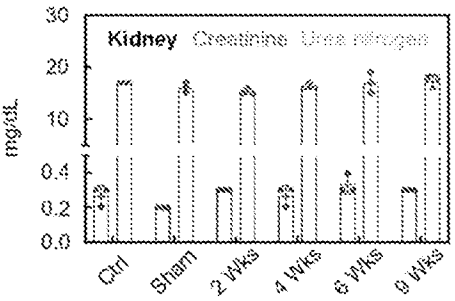


FIGURE 6H

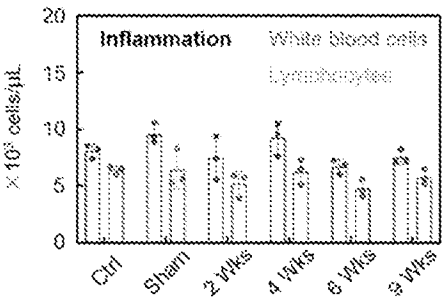


FIGURE 6I

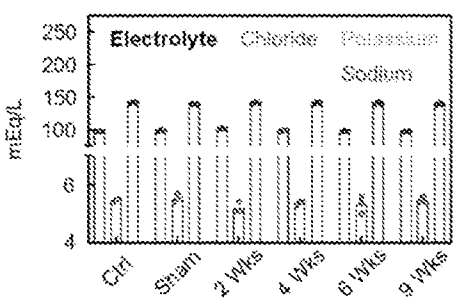


FIGURE 6J

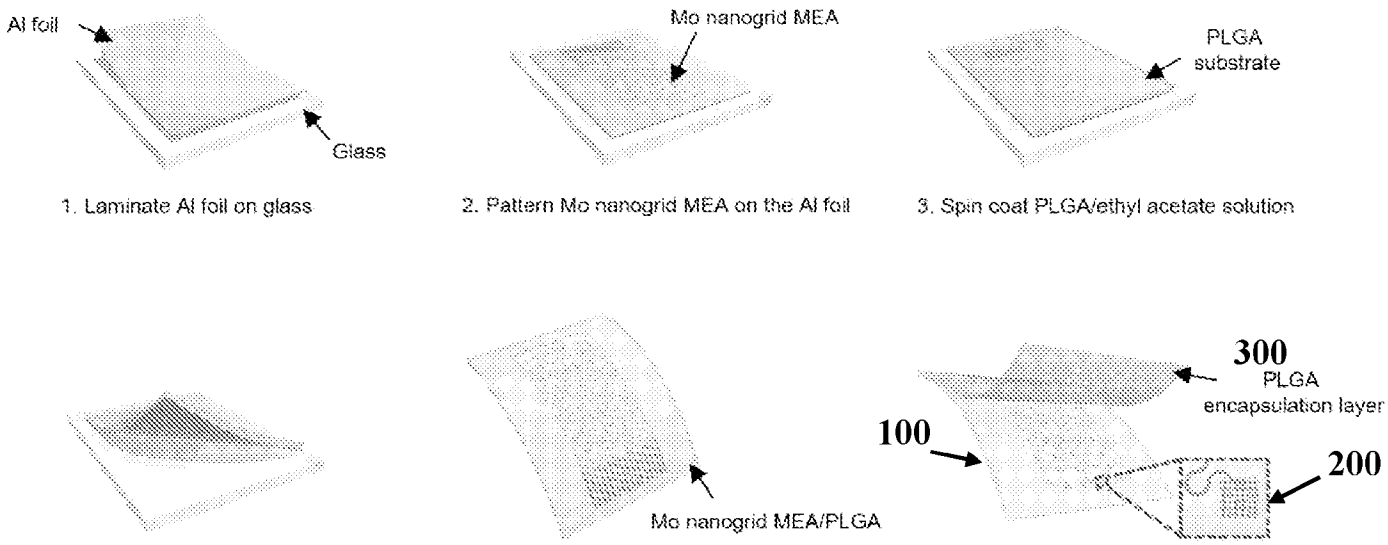


FIGURE 7

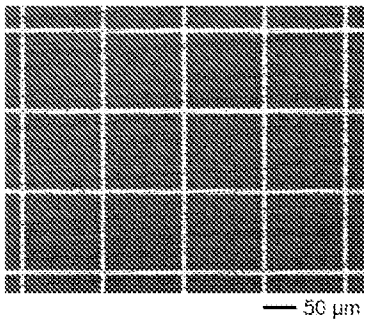


FIGURE 8A

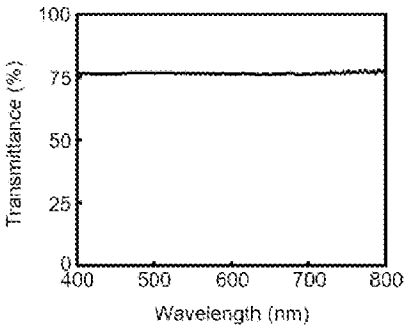


FIGURE 8B

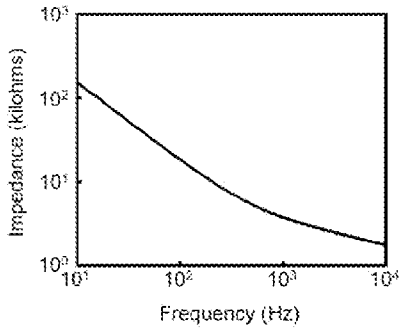


FIGURE 8C

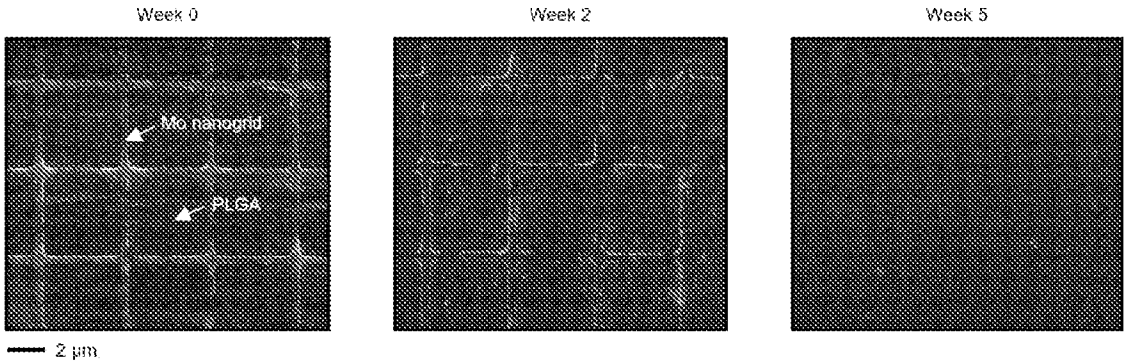


FIGURE 9

FIGURE 10A

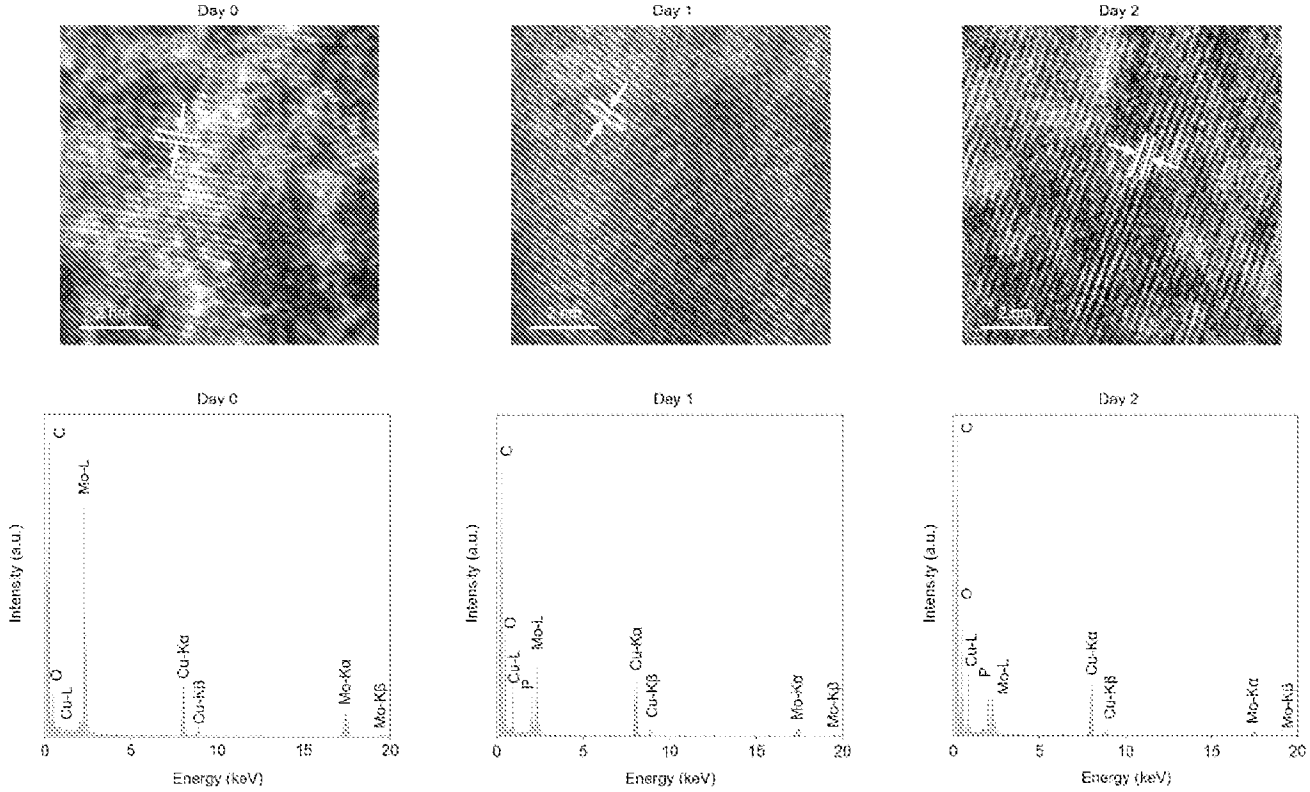


FIGURE 10B

FIGURE 11A

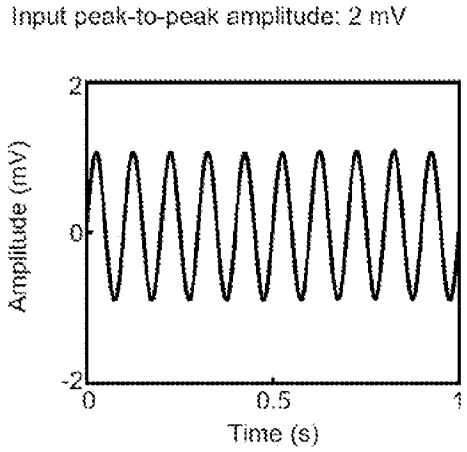
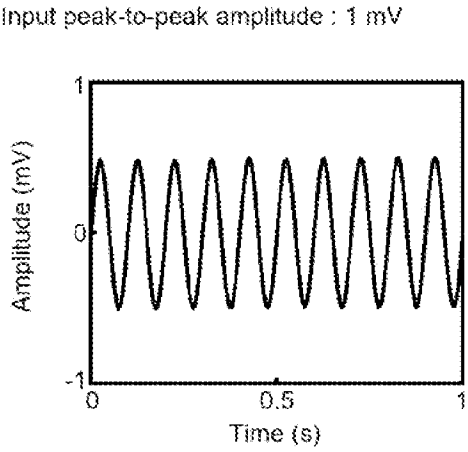


FIGURE 11B



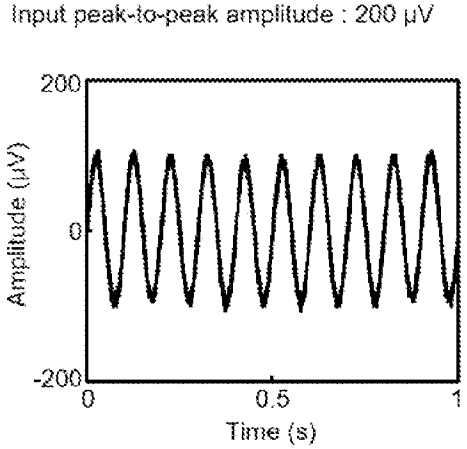


FIGURE 11C

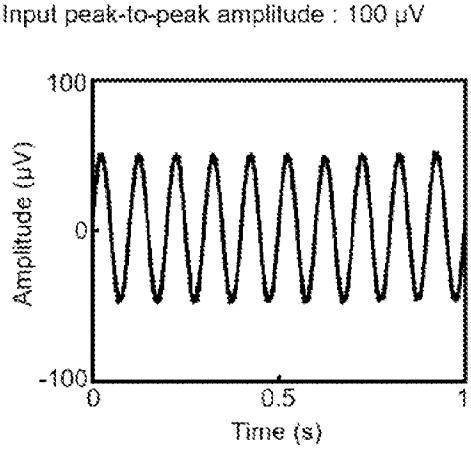


FIGURE 11D

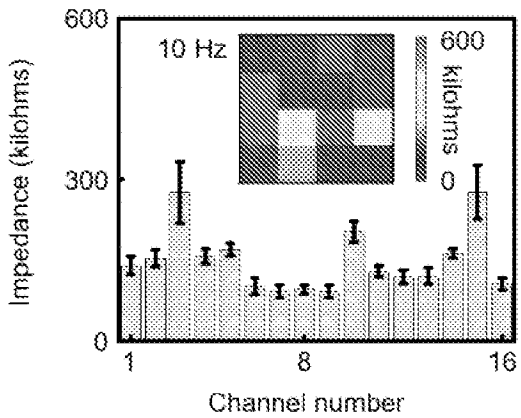


FIGURE 12

FIGURE 13A FIGURE 13B FIGURE 13C FIGURE 13D

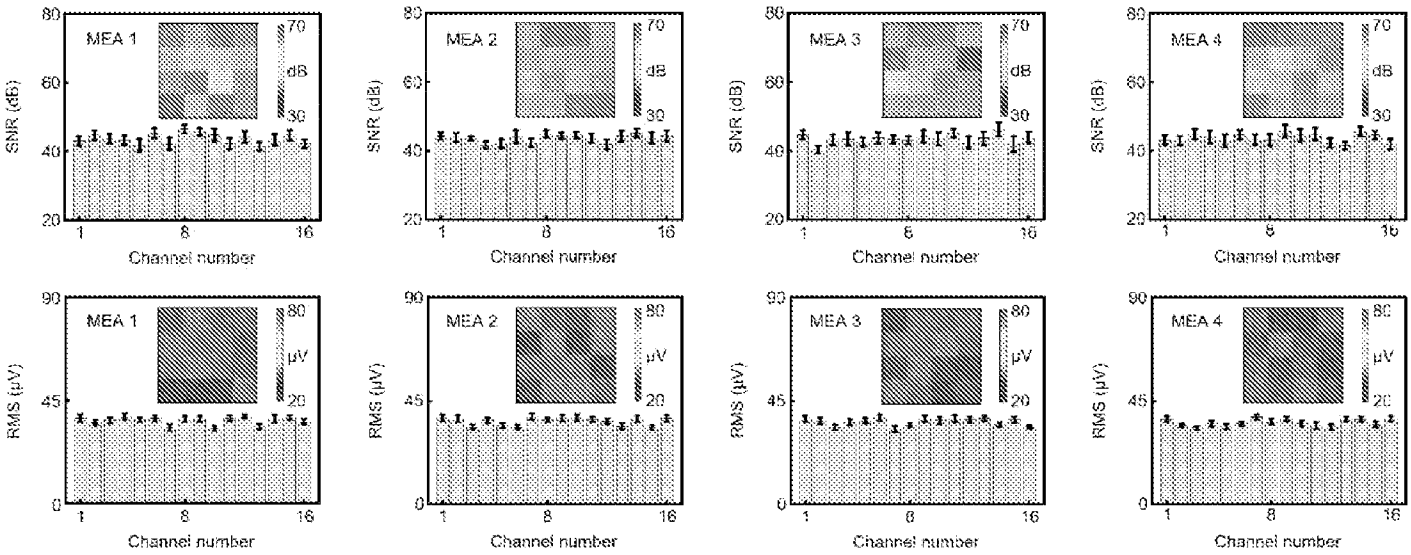


FIGURE 13E FIGURE 13F FIGURE 13G FIGURE 13H

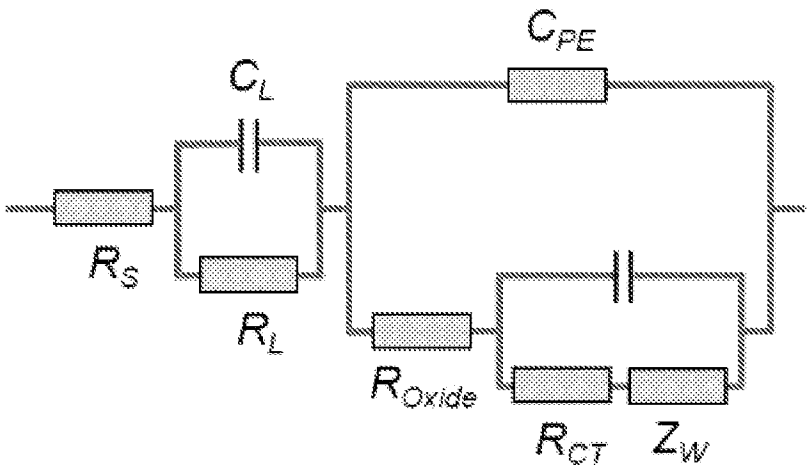


FIGURE 14

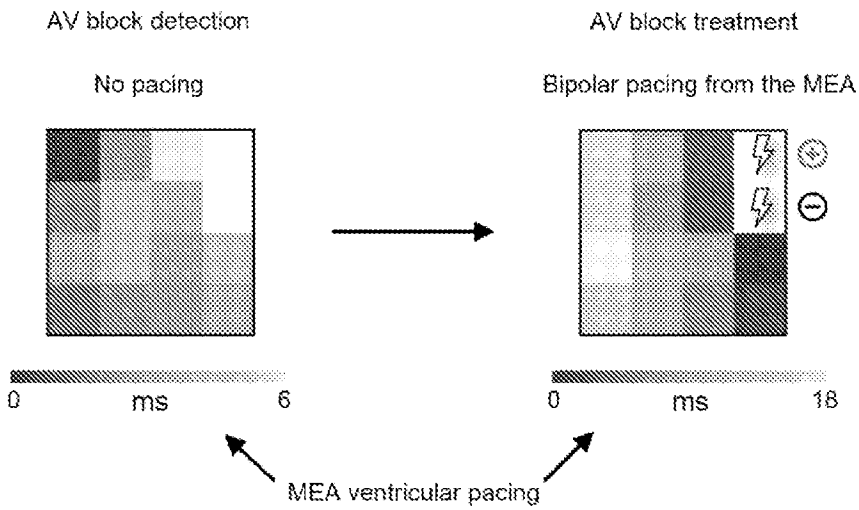


FIGURE 15

FIGURE 16A

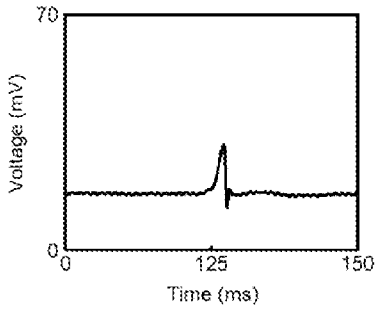
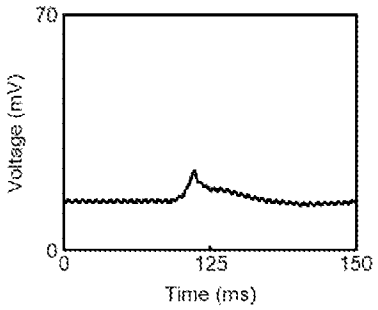


FIGURE 16B



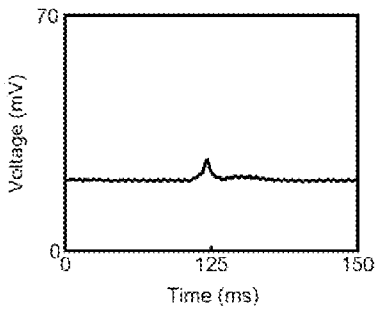


FIGURE 16C

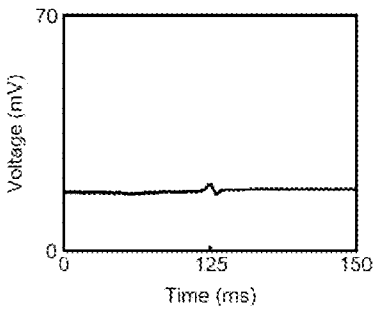


FIGURE 16D

FIGURE 17A

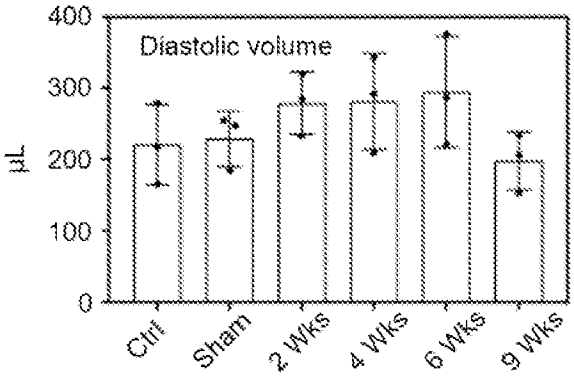
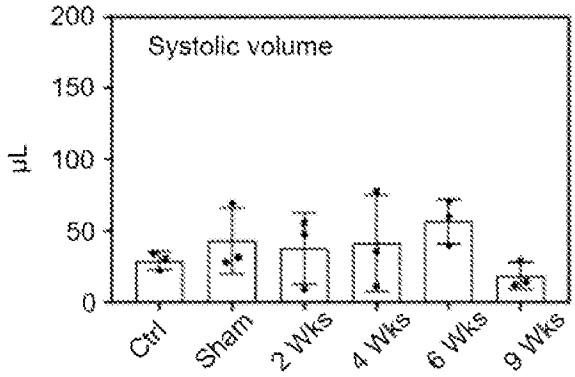


FIGURE 17B



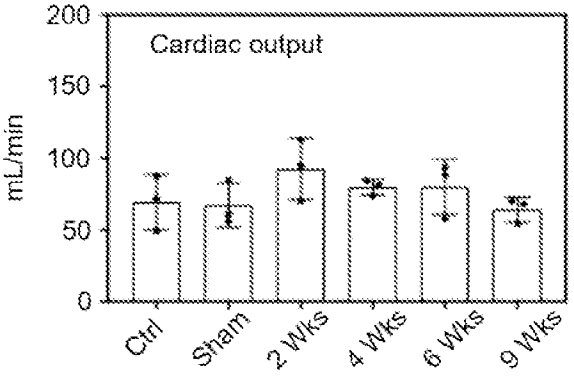


FIGURE 17C

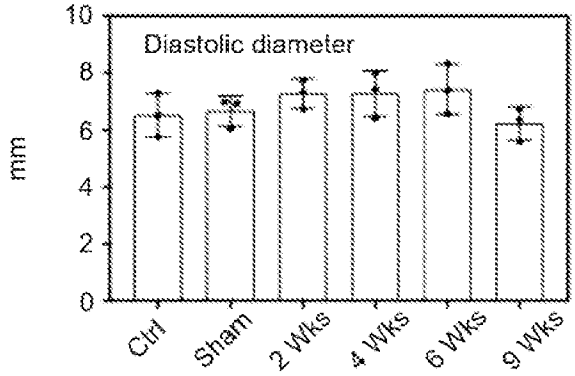


FIGURE 17D

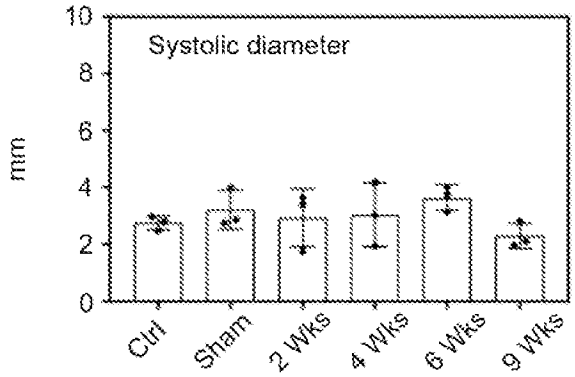


FIGURE 17E

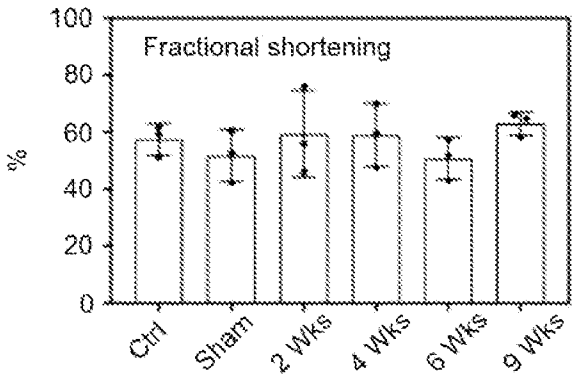


FIGURE 17F

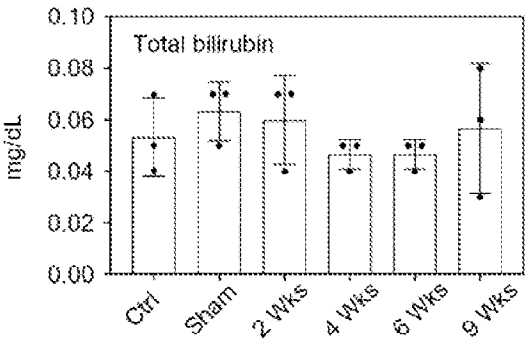


FIGURE 18A

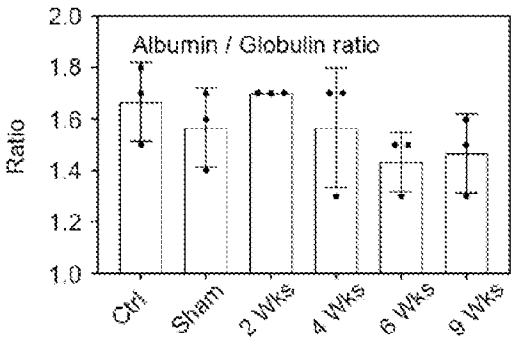
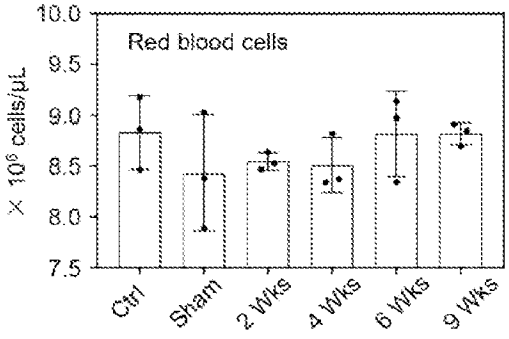
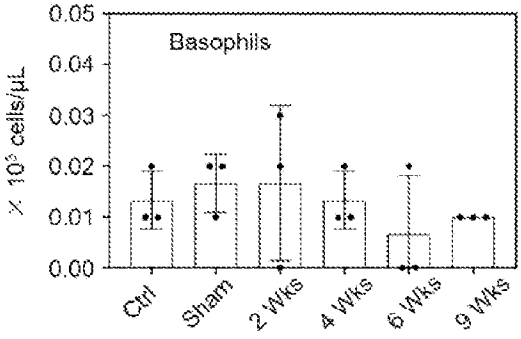


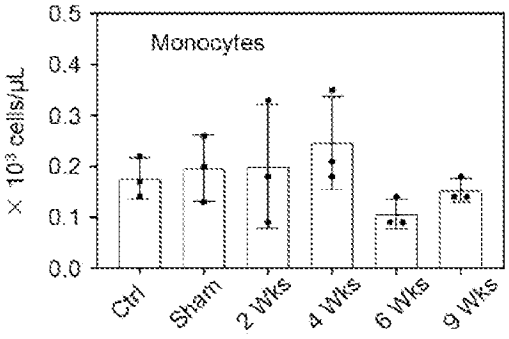
FIGURE 18B

FIGURE 19A

FIGURE 19B







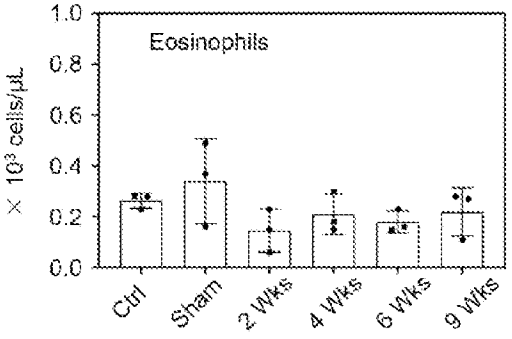


FIGURE 19C

FIGURE 19D

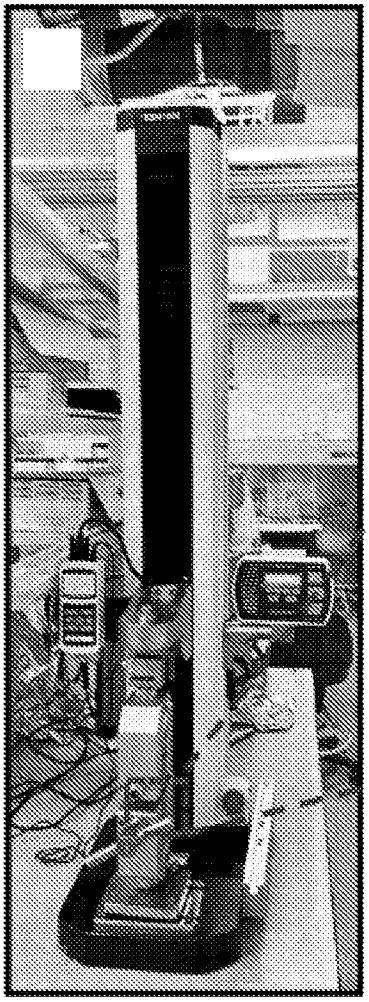


FIGURE 20A

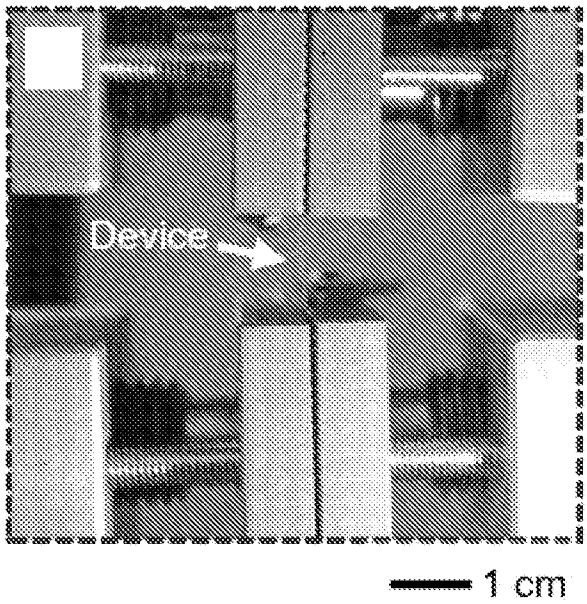


FIGURE 20B

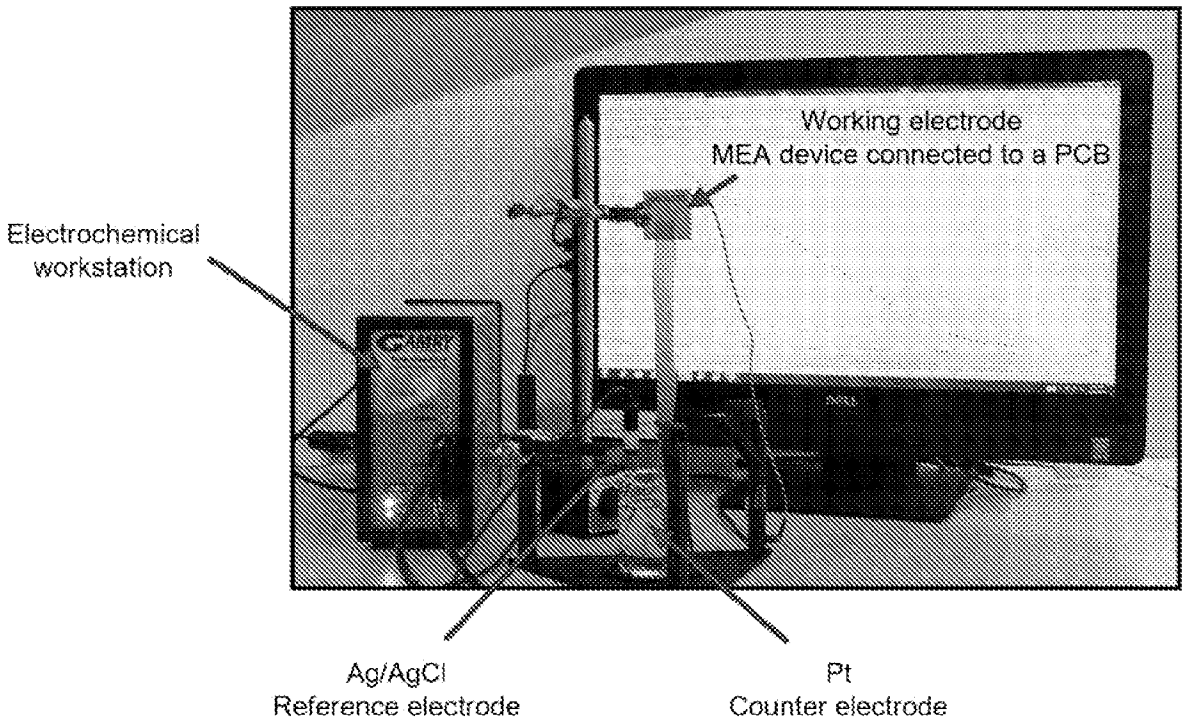


FIGURE 21

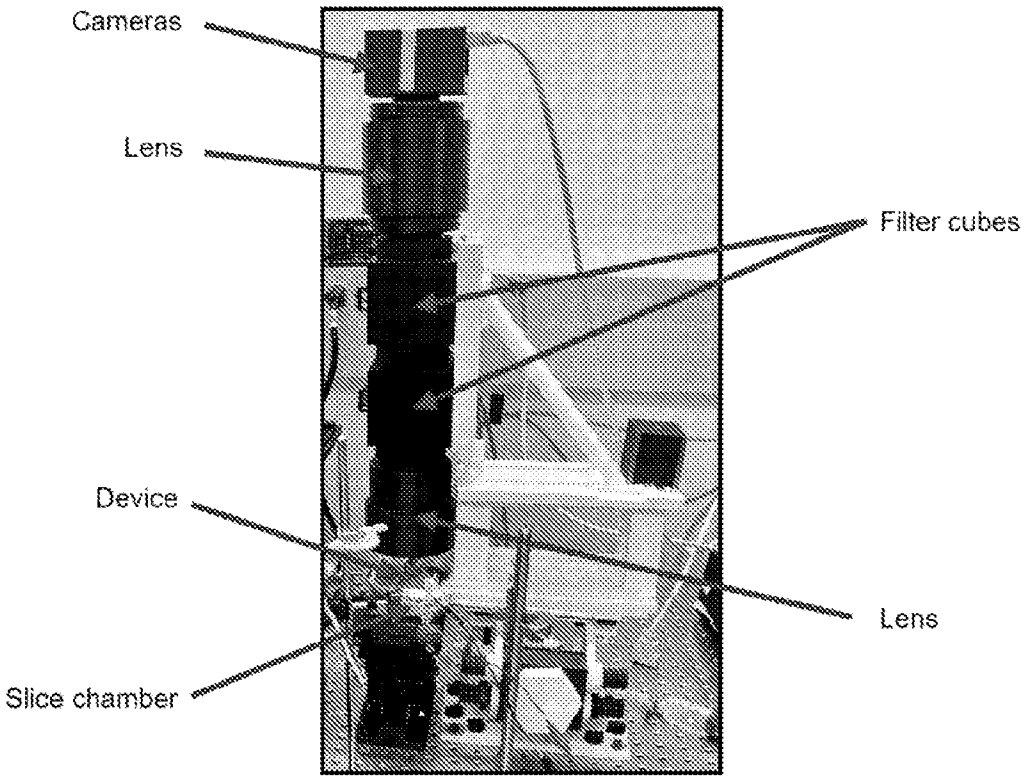


FIGURE 22